# Geophysical Journal International

Advancing Astronomy and Groupington

Geophys. J. Int. (2023) 232, 128–146 Advance Access publication 2022 August 30 GJI Geodynamics and Tectonics https://doi.org/10.1093/gji/ggac332

## A simple force balance model of subduction initiation

Yida Li and Michael Gurnis

Seismological Laboratory, California Institute of Technology, Pasadena, CA 91125, USA. E-mail: vidali@caltech.edu

Accepted 2022 August 19. Received 2022 June 21; in original form 2022 February 21

#### SUMMARY

The initiation and development of subduction zones are associated with substantial stress changes both within plates and at plate boundaries. We formulate a simple analytical model based on the force balance equation of a subduction zone, and validate it with numerical calculations of highly non-linear, coupled thermomechanical system. With two kinds of boundary conditions with either fixed velocity or fixed force in the far-field, we quantitatively analyse the role of each component in the force balance equation, including slab pull, interplate friction, plate bending and basal traction, on the kinematics and stress state of a subducting plate. Based on the numerical and analytical models, we discuss the evolution of plate curvature, the role of plastic yielding and elasticity, and how different factors affect the timing of subduction initiation. We demonstrate with the presence of plastic yielding for a plate of thickness, H, that the bending force is proportional to  $H^2$ , instead of  $H^3$  as previously thought. Although elasticity increases the force required to start nucleating subduction it does not substantially change the total work required to initiate a subduction zone when the yielding stress is small. The analytical model provides an excellent fit to the total work and time to initiate subduction and the force and velocity as a function of convergence and time. Plate convergence and weakening rate during nucleation are the dominant factors influencing the force balance of the plate, and 200 km of plate convergence is typically required to bring a nascent subduction zone into a self-sustaining state. The closed-form solution now provides a framework to better interpret even more complex, time-dependent systems in three dimensions.

**Key words:** Plate motions; Dynamics of lithosphere and mantle; Lithospheric flexure; Mechanics, theory, and modelling; Rheology: crust and lithosphere; Subduction zone processes.

## 1 INTRODUCTION

The balance of forces within subduction zones is a key determinant governing plate motions instantaneously and over time as plates evolve. The force balance likely changes substantially with commensurate changes in the state of stress within plates in time and space, especially during the initiation of a new subduction zone. As deduced from field observations and mechanical models, a subducting plate may experience a change from compression to extension during subduction initiation, which could suggest a transfer of driving force from far-field compression to slab pull. In addition to driving forces, there are factors that resist plate motion, such as friction at the subduction interface and rigid plate bending. While bending, the viscous plate experiences deformation within the plate hinge zone, with considerable energy dissipated with a force required to counterbalance the bending torque. Other sources of driving and resisting forces, including a traction from flow beneath lithosphere and horizontal pressure changes from the lateral variations of isostatic columns, might also be important components of the force balance.

Despite a considerable literature documenting the key forces which may exist as a function of time using sophisticated numerical methods (Gurnis *et al.* 2004; Nikolaeva *et al.* 2010; Leng & Gurnis 2015; Zhong & Li 2019; Arcay *et al.* 2020), we are not aware of a simple closed form, analytical model of the force balance as a function of time. Although earlier work described instantaneous force balances (McKenzie 1977; Mueller & Phillips 1991), none has been formulated in time. Such a model provides a guide to better understand the complex, time-dependent phenomena that occur in the full solution of the coupled non-linear conservation equations. Here we derived the relationship between forces and plate motion in a trench perpendicular cross section based on a force balance equation, and later validate the result against the full solution of the coupled system of equations with a suite of numerical computations. The role of elasticity is shown through comparison of solutions with and without elasticity.

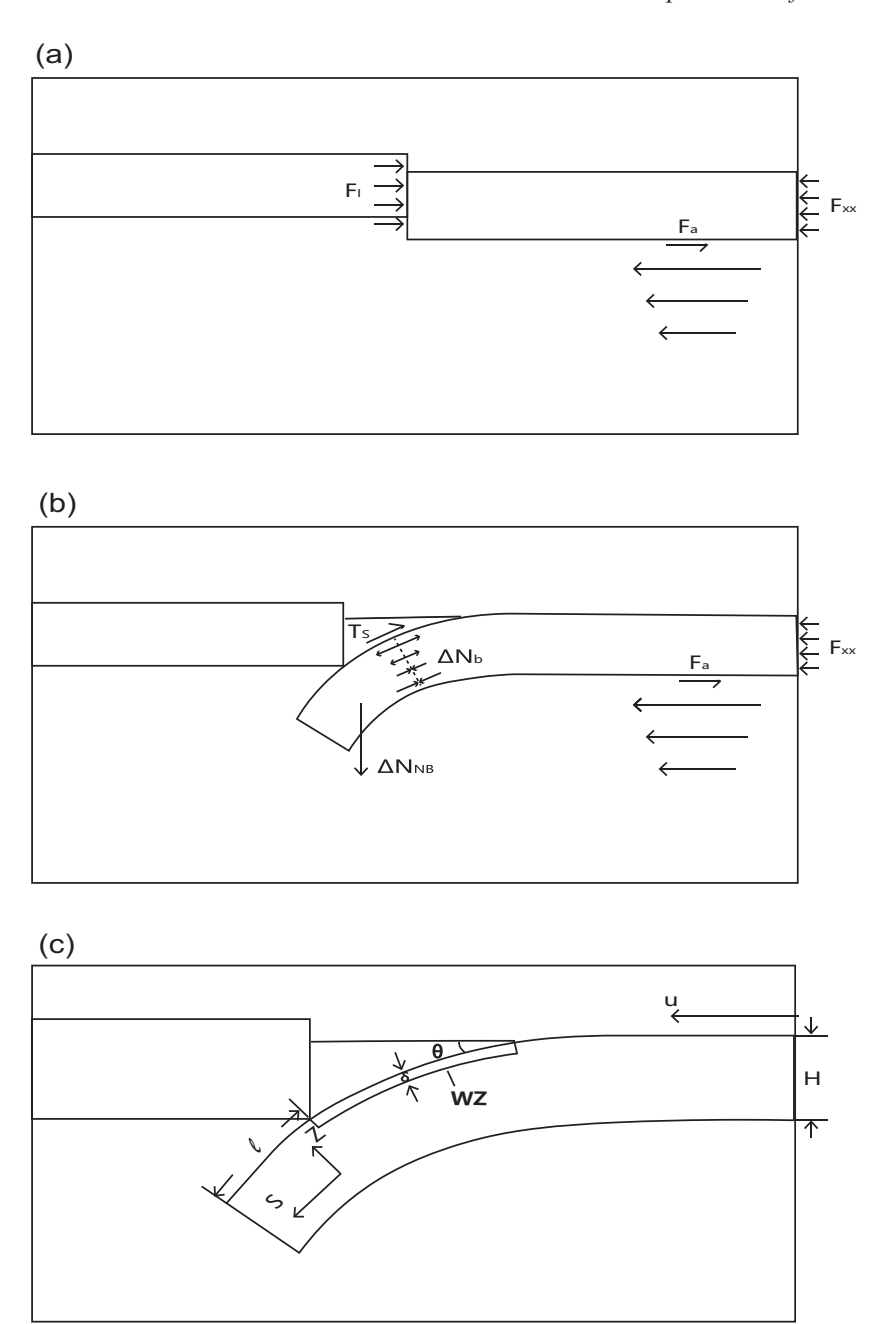


**Figure 1.** Cross-sectional schematic of the force balance showing (a) the initial condition and (b) during an advanced stage of subduction initiation with details shown in (c) (illustrating the local (z - s) coordinate system). WZ denotes the weak zone.

## 2 FORCE BALANCE

At any instant of time, the force balance for a viscously dominated plate is

$$F_{xx} + \Delta N_{\text{NB}} = \Delta N_{\text{b}} + T_{\text{S}} + F_{\text{a}} + F_{\text{I}},\tag{1}$$

where  $F_{xx}$  is an applied far-field compression,  $\Delta N_{\rm b}$  and  $\Delta N_{\rm NB}$  are the change in the normal force arising from the bending of the slab and negative buoyancy, respectively, from the slab tip to the surface (Buffet 2006),  $T_{\rm S}$  is the frictional resistance between the slab and the over-riding plate,  $F_{\rm a}$  is resistance from viscous shear in the asthenosphere and  $F_{\rm I}$  is a resistance from a horizontal pressure gradient across the plate boundary arising from differing isostatic columns (Fig. 1a). In Appendix A, we provide a detailed derivation of this equation. One can see that  $F_{\rm I}$  has been added as a resisting force, not as a driving force for subduction initiation, as previously considered in the literature (Nikolaeva *et al.* 2010; Leng & Gurnis 2015). Below, we will discuss this further, but detailed computations in 2-D show that  $F_{\rm I}$  initially causes the in-coming plate to slow.

There are two forces within the slab (Fig. 1b) that act in the downdip direction. The first is a driving force from the negative buoyancy of the slab

$$\Delta N_{\rm NB} = H \Delta \rho g \sin \theta \cdot \ell, \tag{2}$$

where H is the plate thickness, g the acceleration of gravity,  $\Delta \rho$  the density difference between slab and ambient mantle,  $\theta$  dip angle of the slab (typically increasing from 0 at the trench to 45° in the subduction zone) and  $\ell$  the horizontal cumulative slab (plate) displacement. The second is a resisting force generated from bending, which has previously been considered, for example in Buffet (2006) as an equation tracking the total normal force change attributed to the bending of a thin viscous plate of constant viscosity

$$\Delta N_{\rm b} = \frac{1}{3} \eta H^3 \int_0^L \left(\frac{\mathrm{d}k}{\mathrm{d}s}\right)^2 \mathrm{d}s \cdot u = K_{\rm b} u,\tag{3}$$

where k is the local curvature of the bending slab,  $\eta$  the viscosity of the slab, u the convergence velocity at the nascent trench (so that,  $u = \dot{\ell}$ ), s the distance along the plate's centre line (Fig. 1c) and L the total length of centre line. A single coefficient, which we call  $K_b$ , can be used to collapse all coefficients associated with bending into a single term that multiplies u. As the effective viscosity of the bending plate could change as the new subduction zone develops, the constant viscosity assumption (and hence the validity of the equation) will be critically evaluated with detailed computations. In calculations, we will consider the more realistic case when the effective viscosity of the plate no longer remains constant, specifically when the plate experiences brittle failure. We consider a constant yield stress for the plate, accomplished through a reduction in viscosity.

For the plate bending problem, the hinge zone is where a great amount of deformation occurs and experiences a reduction of effective viscosity due to plastic failure. In Appendix B, we show that the contribution of a bending torque from the hinge zone is no longer proportional to the convergent velocity u, but rather a constant independent on u. Combining the contributions of brittle and ductile deformation, the total bending torque is

$$\Delta N_{\rm b} = K_{\rm b} u + N_{\rm HZ},\tag{4}$$

where  $N_{\rm HZ}$  is the bending torque from the hinge zone, a parameter independent of u.  $K_{\rm b}u$  accounts for the contribution of bending force from the area where the bending is not large enough to cause plasticity. For a relatively small yielding stress, plasticity occurs almost everywhere in the bending area, therefore  $N_{\rm HZ} > > K_{\rm b}u$ . The bending torque in the hinge zone is expressed as

$$N_{\rm HZ} = \frac{1}{6}H^2(\mathrm{d}k/\mathrm{d}z)_{\rm max}s_{\rm HZ}\tau_{\rm max},\tag{5}$$

where  $(dk/ds)_{max}$  is the maximum rate of plate curvature change.  $s_{HZ}$  is the width of the hinge zone and  $\tau_{max}$  the maximum yield stress in the plate.

The resistance at the base of the subducting plate during convergence is

$$F_{\mathbf{a}} = 2\eta_{\mathbf{a}}\dot{\varepsilon}L_{p} = \eta_{\mathbf{a}}\frac{u}{d} \cdot L_{p} = \eta_{\mathbf{a}}\frac{L_{p}}{d}u,\tag{6}$$

where  $\eta_a$  is the viscosity of the asthenosphere,  $d_a$  the thickness of the asthenosphere and  $L_p$  the length of the plate.

The plate is also resisted by the total friction at the plate boundary,  $T_{\rm S}$ , a process that is primarily limited by the yield stress which in turn is controlled by strain weakening. In the numerical model, we consider plastic failure to be governed by a Drucker–Prager yielding criteria with a maximum stress as the upper limit,  $\tau_y = \min(\mu_y p + C, \tau_{y0})$ , where p is hydrostatic pressure. For the weakening, we use a simplified two-stage process to represent the strain weakening: Initially the yielding parameters  $\mu_y$  and C decrease linearly with the accumulation of plastic strain, but once the plastic strain saturates, that is the plastic strain exceeds the reference plastic strain,  $\varepsilon_{P0}$ , the yielding stress remains at  $\tau_{yf}(\mu_{yf} = 0, C_f = \tau_{yf})$ . For the analytical solution, the two stage process is further simplified as  $\tau_y = \tau_{\rm max}$  prior to plastic saturation and  $\tau_y = \tau_{yf}$  after saturation. This approximation is valid because p is typically much greater than  $\tau_{y0}$  so that the non-saturated yield stress ( $\mu_y > 0$ ) is mostly cut-off by  $\tau_{v0}$ . Prior to strain saturation of the fault, the total shear stress from the fault is

$$T_{\rm S} = \int_0^{\frac{H}{\sin\theta}} \tau_y \mathrm{d}s = \left(\tau_{y0} + \frac{(\tau_{yf} - \tau_{y0})\ell}{\delta\varepsilon_{P0}}\right) \frac{H}{\sin\theta} + \ell \frac{\tau_{y0} - \tau_{yf}}{\delta\varepsilon_{P0}} \ell = A - B\ell + C\ell^2,\tag{7}$$

where  $A = \frac{\tau_{y0}H}{\sin\theta}$ ,  $B = \frac{\tau_{y0}}{\delta\varepsilon_{P0}} \cdot \frac{H}{\sin\theta}$  and  $C = \frac{\tau_{y0}}{\delta\varepsilon_{P0}}$ . After the strain saturates, that is  $\ell > \delta\varepsilon_{P0}$ , where  $\delta$  is the fault thickness,  $T_{\rm S}$  becomes

$$T_{\rm S} = \int_0^{\frac{H}{\sin \theta}} \tau_{\rm y} \mathrm{d}s = \tau_{\rm yf} \frac{H}{\sin \theta} + \delta \varepsilon_{P0} (\tau_{y0} - \tau_{yf}) = D. \tag{8}$$

The isostatic force,  $F_{\rm I}$ , is caused by the horizontal pressure difference across the different density columns making up the plate boundary. As a result of isostasy, the horizontal pressure gradient is zero below the compensation depth,  $d_{\rm comp}$ , at the base of the lithosphere. However, above the compensation depth, the pressure at the same depth is not usually equal because of density differences in adjacent columns. Here, the density arise from both thermal and compositional differences. Assuming the plate thermal structure obeys a half-space cooling model, the total thermal plate boundary force is the integration of pressure differences from the thermal contrast over depth (Turcotte & Schubert

1982, eq. 6.405)

$$F_{\text{therm}} = \int_0^{d_{\text{comp}}} \Delta P dz = g \rho_{\text{m}} \alpha \Delta T \left( 1 + \frac{2\rho_{\text{m}} \alpha \Delta T}{\pi (\rho_{\text{m}} - \rho_{\text{w}})} \right) \kappa (t_2 - t_1), \tag{9}$$

where  $\rho_{\rm m}$  is the mantle reference density,  $\rho_{\rm w}$  is the water density,  $\alpha$  is the coefficient of thermal expansion,  $\Delta T$  is the temperature difference between mantle and surface,  $\kappa$  is the thermal diffusivity and  $t_1$  and  $t_2$  are the plate age of plate 1 and plate 2, corresponding to the overriding plate and subducting plate, respectively. The other factor contributing to the pressure gradient is the difference in composition between the two plates, assumed to be limited to the crust for simplicity. Similarly, we obtain the boundary force from compositional density differences

$$F_{\text{comp}} = \int_{0}^{d_{\text{comp}}} \Delta P \, dz = \frac{1}{2} g \frac{(\rho_{\text{m}} - \rho_{C1})(\rho_{C1} - \rho_{\text{w}})}{\rho_{\text{m}} - \rho_{\text{w}}} \Delta C_{1}^{2} - \frac{1}{2} g \frac{(\rho_{\text{m}} - \rho_{C2})(\rho_{C2} - \rho_{\text{w}})}{\rho_{\text{m}} - \rho_{\text{w}}} \Delta C_{2}^{2}, \tag{10}$$

where  $\rho_{C1}$ ,  $\rho_{C2}$  are the crustal density of plate 1 and plate 2, and  $\Delta C_1$  and  $\Delta C_2$  are the crustal thickness of plate 1 and plate 2. With the joint contribution of thermal and compositional density differences across the plate boundary, the total isostatic force at the plate boundary is

$$F_{\rm I} = F_{\rm therm} + F_{\rm comp}. \tag{11}$$

Substituting in the expressions of  $\Delta N_{\rm b}$ ,  $F_{\rm NB}$ ,  $T_{\rm S}$  and  $F_{\rm a}$  as given above, eq. (1) yields

$$F_{xx} + H\Delta\rho g\sin\theta \cdot \ell = T_{\rm S} + \eta_a \frac{L_P}{d_a} \cdot u + F_{\rm I} + K_{\rm b}u + N_{\rm HZ}. \tag{12}$$

The completeness of the force balance equation is examined with solutions as time progresses during subduction initiation, assuming two typical scenarios, one with plate convergence driven by velocity boundary conditions and another driven by force boundary conditions. These will form the basis for comparison against solutions for the fully coupled, non-linear equations.

## 2.1 Velocity boundary condition

With a velocity boundary condition,  $u = u_0$ , the plate convergence is driven by a fixed, constant velocity and eq. (12) becomes

$$F_{xx} = \left(\eta \frac{L_P}{d_a} + K_b\right) u + T_S - H\Delta\rho \sin\theta\ell + N_{HZ} + F_I. \tag{13}$$

With eq. (7) and (8), (13) yields

$$F_{xx} = \begin{cases} A\ell^2 - (B + H\Delta\rho\sin\theta)\ell + C + (\eta\frac{L_P}{d_a} + K_b)u_0 + T_S + N_{HZ} + F_I, & \ell < \delta\varepsilon_{P_0} \\ -H\Delta\rho\sin\theta \cdot \ell + D + (\eta\frac{L_P}{d_a} + K_b)u_0 + T_S + N_{HZ} + F_I, & \ell > \delta\varepsilon_{P_0}. \end{cases}$$
(14)

We will discuss the nature of these solutions when comparisons are made to the full solution of the governing equations from the numerical model.

## 2.2 Force boundary condition

Alternatively, we apply a constant far-field compression  $F_{xx}$  that drives the plate motion, so that the convergence velocity becomes

$$u = \frac{F_{xx} + H\Delta\rho g\ell \sin\theta - T_{S} - F_{I} - N_{HZ}}{K_{b} + \eta_{a} \frac{L_{P}}{ds}}.$$
(15)

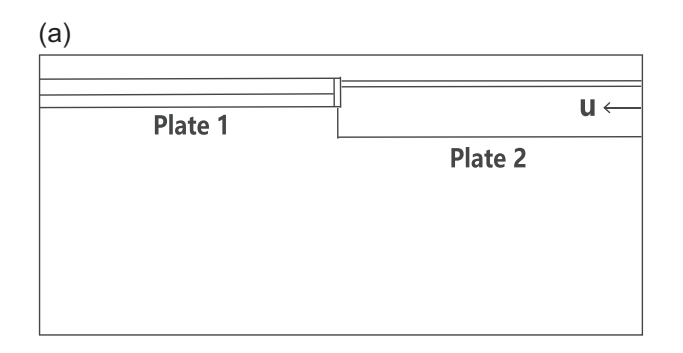
Based on this equation, we obtain the relationship between time t taken to reach a horizontal displacement of  $\ell$  through the integration  $t = \int_0^\ell \frac{\mathrm{d}\ell'}{u}$ . The expression of t with respect to  $\ell$  depends on how much strain has accumulated within the fault zone: When  $\ell < \varepsilon_{P_0} \delta$ 

$$t \approx \frac{4K_1C\ell}{B_1^2 + 4C(F_{xx} - A - F_1 - N_{HZ})},\tag{16}$$

where  $K_1 = K_b + \frac{L_P}{d_a} \cdot \eta_a$ . When  $\ell > \delta \varepsilon P_0$ 

$$t \approx \frac{4K_1\tau_{y0}}{B_1^2 + 4C(F_{xx} - A - F_1 - N_{HZ})} + \frac{K_2(\ell - \delta\varepsilon_{P0})}{F_{xx} - D - F_1 - N_{HZ}},$$
(17)

where  $B_1 = B + H\delta\rho g\sin\theta$ ,  $K_2 = K_b + \frac{L_P}{d_a} \cdot \eta_a$ .  $K_1$  and  $K_2$  follow the same definition, but due to the asthenosphere viscosity  $\eta_a$  is non-Newtonian, the second stage  $(\ell > \delta \varepsilon_{P0})$  has an overall lower  $\eta_a$  due to the higher plate speed and  $K_2$  is thereby smaller than  $K_1$ . In eq. (16) and (17) we only present the approximate forms, with the detailed derivations and full expressions given in the Supporting Information (eqs S.1 and S.2). We will discuss solutions of these equations with the force boundary conditions when comparing against the solution of the full equations with the numerical models.



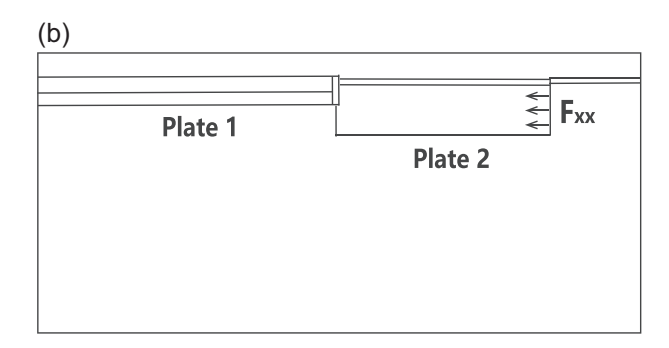


Figure 2. The model setup for models with a velocity boundary conditions and b force boundary conditions. Plate 1 and Plate 2 corresponding to the overriding plate and subducting plate.

## 3 MODEL SETUP

We have formulated a series of computations in a 2-D domain with the finite element method using the *Underworld* package (Mansour *et al.* 2020) to validate the simple force balance. Computational models with both viscoplastic and viscoelasto—plastic rheologies are used to isolate the role of elasticity during subduction initiation. Initial temperature field is from half-space-cooling model with given subducting and upper plate age. Models are computed with both imposed velocities and imposed forces, so as to mimic the routes taken in the simple analytical force balance. The models with imposed velocities are implemented using a Dirichlet condition on the right wall through the depth of the plate (Fig. 2a). The models with imposed forces are implemented by applying a horizontally acting body force through a narrow column (Fig. 2b) on the right edge of the subducting plate, following Leng & Gurnis (2011), and the thermal age of the rightmost 100 km lithosphere is set to be 0, decoupling the subducting plate from the model domain boundary. With the large topographic gradients rapidly developing during subduction initiation, the topography is tracked as a free surface, as in previous studies (Toth & Gurnis 1998; Gurnis *et al.* 2004; Nikolaeva *et al.* 2010). Here, the free surface is approximated by overlaying the plates with a 40 km thick, low viscosity (e.g. sticky-air) layer (Crameri *et al.* 2012). The material has a non-Newtonian and temperature-dependent rheology

$$\eta(T, \dot{\varepsilon}) = \eta_0 e^{\frac{E}{nRT} - \frac{E}{nRT_0}} \left(\frac{\dot{\varepsilon}}{\dot{\varepsilon}_0}\right)^{\frac{1-n}{n}},\tag{18}$$

where E is the activation energy, R the ideal gas constant and n the exponent of non-Newtonian flow.  $\eta_0$  is the reference viscosity at a the reference temperature,  $T_0$ , and reference strain rate,  $\dot{\varepsilon_0}$ . In addition to the non-Newtonian viscosity, the material yields (plastic failure) by imposing an upper limit on the stress; the effective viscosity becomes

$$\eta_{\text{eff}} = \min \left( \eta(T), \tau_y / \dot{\varepsilon}_{\text{II}} \right), \tag{19}$$

where  $\tau_y$  is the yield stress and  $\dot{\epsilon}_{\rm II}$  is the square root of the second invariant of strain rate tensor. The effective viscosity is confined by minimum and maximum values (Table 1). The yield stress follows the Drucker–Prager yielding criteria with a upper cut-off,  $\tau_y = \min(\mu_y p + C, \tau_{y0})$ .

Weakening processes are approximated by reducing the yield stress with plastic strain, following a two stage process: Prior to a strain saturation, C and  $\mu_y$  linearly decreases with accumulation of plastic strain  $\varepsilon_P$ , and afterwards  $\tau_y$  remains constant.

$$\tau_{y} = \begin{cases} \mu_{y}p + C, & \varepsilon_{P} \leq \varepsilon_{P0} \\ \tau_{yf}, & \varepsilon_{P} > \varepsilon_{P0}, \end{cases}$$
(20)

where  $\varepsilon_{P0}$  is the reference plastic strain that controls the rate of weakening. C and  $\mu_y$  are cohesion and friction coefficient,  $C = (\tau_{yf} - C_0)\frac{\varepsilon_P}{\varepsilon_{P0}} + C_0$  and  $\mu_y = \mu_{y0} - \mu_{y0}\frac{\varepsilon_P}{\varepsilon_{P0}}$ . The material within the majority of the domain is governed by non-Newtonian flow, indicating the dominance of ductile deformation. In two regions, the weak zone and hinge zone, where the strain rate is large, the yielding dominates, indicating the deformation makes a transition into brittle failure. Three materials are present within the domain: An 8-km-thick basaltic crust on top of the subducting plate that can metamorphose to eclogite at depth (Hacker *et al.* 2003); a 25-km-thick granitic crust on top of the

Table 1. Model parameters.

Symbol	Definition	Value	Symbol	Definition	Value
n	Non-Newtonian exponent	3	$\tau_{v0}$	Maximum yield stress	150 MPa
E	Activation energy	$540 \text{ kJ mol}^{-1}$	$ au_{vf}$	Minimum yield stress	3 MPa
$\eta_{ m min}$	Minimum viscosity	10 <sup>19</sup> Pa⋅s	$\varepsilon_{P0}$	Reference plastic strain	1 or 2
$\eta_{ m max}$	Maximum viscosity	$10^{25} \text{ Pa} \cdot \text{s}$	$t_1$	Overriding plate age	20 Myr
μ	Shear modulus	$3 \times 10^{10} \text{ Pa}$	$t_2$	Subducting plate age	40 Myr
÷0	Reference strain rate	$10^{-15} \text{ s}^{-1}$	$\Delta C_1$	Continental crustal thickness	25 km
χ	Thermal expansivity	$3 \times 10^{-5} \text{ C}^{-1}$	$\Delta C_2$	Oceanic crustal thickness	8 km
c	Thermal diffusivity	$10^{-6} \text{ m}^2 \cdot \text{s}^{-1}$	Н	Plate mechanical thickness	60 km
$T_0$	Surface temperature	0 °C	δ	Fault thickness	20 km
$\Gamma_1$	Mantle temperature	1400 °C	$\theta$	Fault dip angle	45°
$C_0$	Initial cohesion	44 MPa	$\mu_{v0}$	Initial friction coefficient	0.6
$\eta_{ m st}$	Sticky air viscosity	10 <sup>19</sup> Pa⋅s	$\mu_{ m st}$	Sticky air shear modulus	$3 \times 10^{10} \text{ Pa}$
$d_{\mathrm{st}}$	Sticky air thickness	40 km	κ <sub>st</sub>	Sticky air thermal diffusivity	$10^{-5} \text{ m}^2 \cdot \text{s}^{-1}$

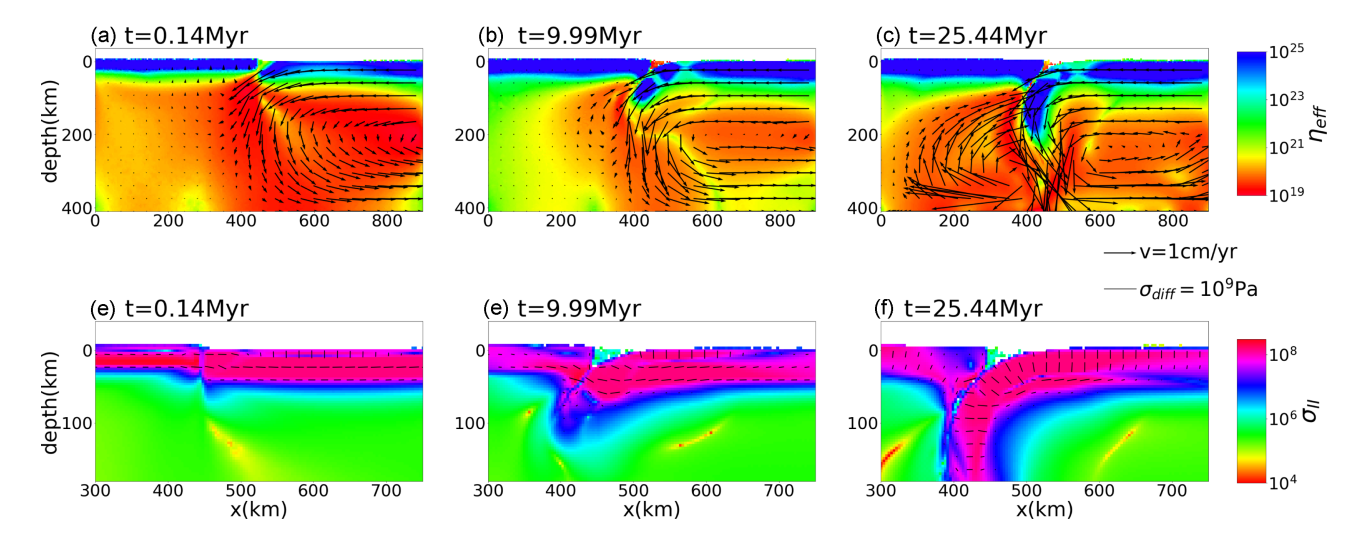


Figure 3. (a)—(c) The effective viscosity [as  $\log_{10}(\eta_{\rm eff})$ ] is colour coded and overlain by the velocity vector at different time from velocity boundary model  $u = 1 \text{ cm yr}^{-1}$ . (d)—(f) The second invariant of stress  $\sigma_{\rm II}$ [as  $\log_{10}(\sigma_{\rm II})$ ] is colour-coded and overlain by the stress bar, from the same model as (a)—(c). The length of the stress bar represent the difference between the largest and smallest principle stress,  $\sigma_{\rm diff}$ , and the direction is the direction of the smallest principle stress (compression axis).

over-riding plate; and an olivine mantle composing the remainder of the domain. The density varies with composition, but the rheological parameters are invariant so as to validate the simple force balance equations.

For models with a velocity boundary condition, we determine the total horizontal compressional force within the plate,  $F_{xx} = -\int_{-\frac{H}{2}}^{\frac{H}{2}} \sigma_{xx} dz$ , with plate convergence  $\ell$ , and compare against the evaluation of eq. (13). For models driven with a force boundary, the plate convergence  $\ell$  versus time from numerical models are compared against evaluation of eqs (16) and (17). In the first set of models (Fig. 2a), the boundary velocity controls plate convergence and the plate motion remains constant with time. In the force boundary model (Fig. 2b), the compression  $F_{xx}$  is applied via a body force in a thin layer on the right-hand end of the subducting slab, and a ridge with 0 thermal age is connected to the right of the subducting slab to decouple the subducting slab from the right wall. The presence of thermal ridge also naturally generate an additional 'ridge push' compression.

#### 4 VALIDATION

## 4.1 Velocity boundary

Subduction initiation with imposed velocity evolves through a pathway (Fig. 3) similar to published models (Gurnis *et al.* 2004; Zhong & Li 2019; Maunder *et al.* 2020). In the case with an imposed velocity of  $u_0 = 1$  cm yr<sup>-1</sup>, the viscosity (Figs 3a–c) is strongly influenced by temperature, but several features stand out. The first is a conspicuous reduction of viscosity beneath the subducting plate and around the slab due to the non-linearity of viscosity. The second is a reduction of viscosity at the plate boundary weak zone and hinge zone due to yielding. Despite yielding and non-linear viscosity, the simple force balance appears to capture the principal physics (Fig. 4).

The horizontal compression within the plate interior,  $F_{xx}$ , shows three stages as a function of plate convergence,  $\ell$ , in both the numerical and analytical solutions (Fig. 4). The parameters used in the analytical solution are given in Table 1. In the earliest stage,  $F_{xx}$  drops steeply with

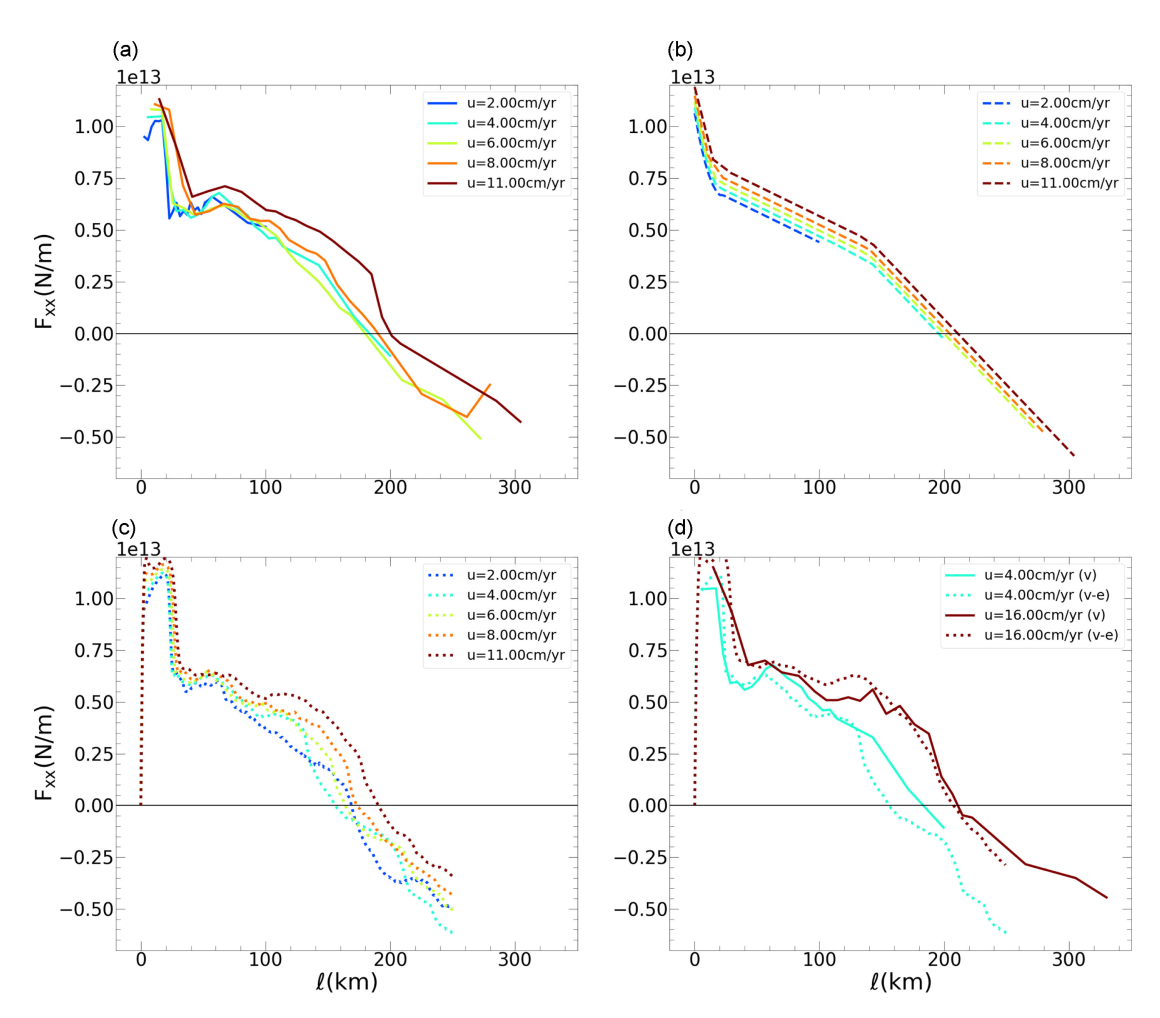


Figure 4. For the velocity boundary models, the force within the plate,  $F_{xx}$ , versus the amount of plate displacement,  $\ell$ . (a) Results from the numerical model with a viscoplastic rheology and different rates of imposed convergence. (b) As in (a), except from the analytical solution. (c) As in (a), except for a viscoelasto-plastic rheology. (d) Comparison of viscoplastic (solid) and viscoelasto-plastic (dotted) rheologies for large and small convergences. The applied plate velocity is encoded by different colours.

plate motion during the first 30 km, followed by a relatively slow drop, and finally after 150 km of convergence the drop accelerates again. The initial rapid stress drop is caused by a reduction of resistant stress from the weak zone,  $T_{\rm S}$ , due to the plastic weakening and the increase of negative buoyancy. In this stage, the whole plate experiences horizontal compression (Fig. 3d). After around 30 km of convergence, the fault zone has been fully weakened and the yield stress no longer decreases. With the reduction of  $T_{\rm S}$ ,  $F_{xx}$  becomes governed by the accumulation of negative buoyancy from plate convergence. By 150 km of convergence, the subducted oceanic crust starts to metamorphose to dense eclogite, accelerating the drop of  $F_{xx}$ . By 200 km convergence,  $F_{xx}$  drops to 0, and the state of stress in the slab and in the incoming plate becomes extensional (Figs 3e and f). The flip in sign of  $F_{xx}$  indicates that subduction has become self-sustaining, the end of the period of subduction initiation,  $t_{\rm SI}$ .

In addition to changes associated with plate convergence,  $\ell$ ,  $F_{xx}$  systematically changes with the convergence velocity,  $u_0$ . From eq. (13), the u-dependence comes from the basal shear  $F_a$  and the bending torque,  $\Delta N_b$ . The non-Newtonian viscosity influences the shear resistance from the base of subducting slab, and with a constant plate velocity (e.g. a constant strain rate at the base of the plate), its role can be more easily isolated. In this model, the effective viscosity at the base of lithosphere is  $10^{19}$  to  $10^{20}$  Pa·s and the estimated basal shear force  $F_a$ , is  $10^{11}$  to  $10^{12}$  N m<sup>-1</sup> (for several cm yr<sup>-1</sup> plate velocity). The normal force from bending,  $\Delta N_b$ , consists of two term:  $N_{\rm HZ}$  from the hinge zone and  $K_b u$  outside of the hinge zone. In the hinge zone, where the flow is dominated by plasticity, the change of normal force is independent of u (Appendix B). Outside of the hinge zone, the plate viscosity is mainly governed by temperature and thereby a constant through the plate, so that the normal force change is only controlled by  $K_b u$ . As the bending barely takes place outside the hinge zone, the contribution of normal force change outside hinge zone is negligible with a fairly small yielding stress ( $K_b u \ll \Delta N_{\rm HZ} \approx 10^{12}$  N m<sup>-1</sup>). For estimating the value, we chose  $K_1 = K_b + \frac{L_P}{d_a} \eta_a \approx 4 \times 10^{20}$  Pa·s (Fig. 4b). In the domain of  $F_{xx} - \ell$ ,  $K_1$  determines the spacing between curves as plate velocity varies (Fig. 4b).

The analytical model is further validated by comparing the spatial variation of the compressional plate normal force  $F_{ss} = -\int_{-H/2}^{H/2} \sigma_{ss} dz$  within the plate for the case  $u_0 = 1$  cm yr<sup>-1</sup> at 15 Myr (Fig. 5). As shown in Appendix A, the change of the compressional plate normal stress  $F_{ss} = -N_b$  is a consequence of basal traction, interplate traction, negative buoyancy, bending torque and isostatic force. We compare the

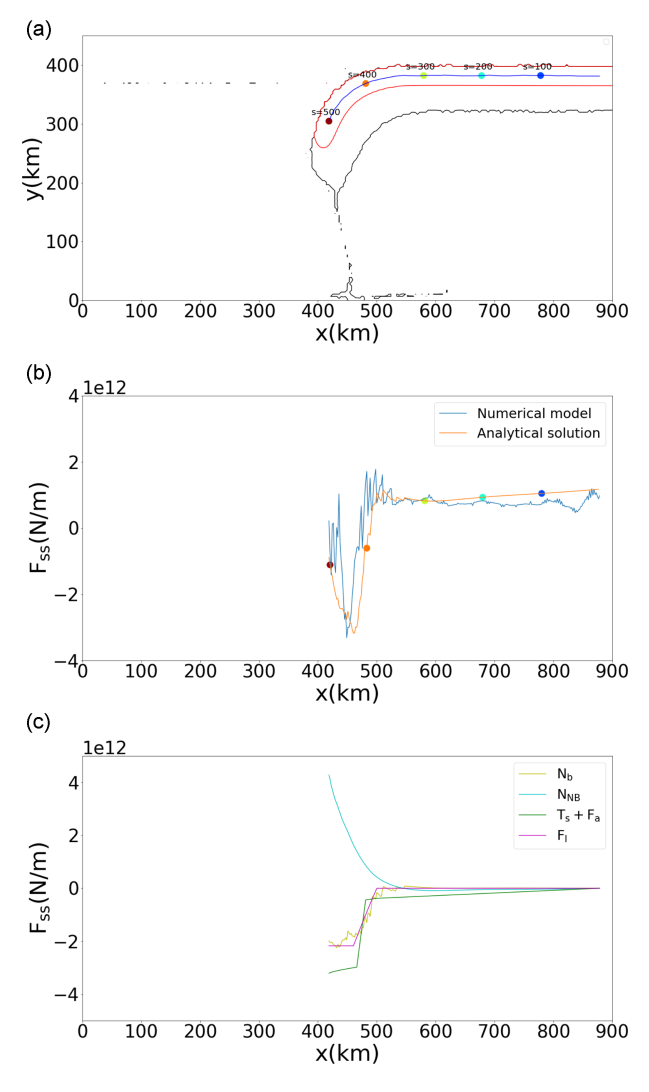


Figure 5. (a) Outline of the thermal plate (in black) and mechanical plate (in red), as well as a curve denoting the plate centre determined from the mechanical plate. (b) The total stress  $F_{ss}$  along the plate from numerical and analytical. (c) The different components making up the bending force predicted by the analytical solution. By the definition of  $F_{ss}$ , positive means compression and negative means extension. As the analytical solution only predicts the change of normal force, all the components of normal force in (c) are fixed on the right end, such that the change along the curves are  $\Delta N_{\rm NB}$  or  $\Delta N_{\rm b}$ . The analytical solution in (b) is the summation of all the component in (c), but a constant is added to align the analytical solution in (b) with the numerical model. The numerical model is with viscoplastic rheology. Static pressure  $P = \int \rho g dz$  is removed in all the measurement of stress.

change of  $F_{ss}$  along the plate from numerical and analytical solutions (Fig. 5b). Different components contributing to the changing  $F_{ss}$  are evaluated analytically (Fig. 5c). The evaluation of  $\Delta N_{\rm NB}$ ,  $F_{\rm a}$ ,  $T_{\rm s}$  and  $F_{\rm I}$  follows the formulations we derived in eq. (2), (6), (7), (8) and (11). For the  $\Delta N_{\rm b}$ , we follow Buffet (2006) and Ribe (2001):

$$\frac{\mathrm{d}N}{\mathrm{d}s} = k \frac{\mathrm{d}M}{\mathrm{d}s},\tag{21}$$

where M is the bending torque  $M = \int_{-H/2}^{H/2} \sigma_{ss} z dz$  and  $N = -F_{ss}$ . Note that the validation of the analytical solution contains the plate curvature k, which is based upon the slab geometry from numerical models. As an example along the centre line temperature contour (T = 600 °C), the measured curvature of the plate is shown in Fig. 5(a), with details in Supporting Information section Evaluating Plate Curvature.

Three principal stages emerge from the variation of  $F_{ss}$  with s (Fig. 5b): From s = 500 to 450 km (note that s is a function of x in Fig. 5(a), as denoted with the coloured filled circles), the plate stress  $F_{ss}$  decrease from 0 at the slab tip into a negative  $F_{ss}$ , an extensional stage driven by negative buoyancy; from s = 450 to 300 km, despite a large negative buoyancy ( $N_{NB}$ ), the interplate friction ( $T_s$ ), is the dominant resisting term, and together with  $F_1$  and  $N_b$ , causes a transition in state of stress from extension to compression. For s < 300 km, there is no substantial bending or slab pull, and so the only term present is the basal shear resistance, which is responsible for the slow increase of  $F_{ss}$  from the plate boundary to its plate interior.

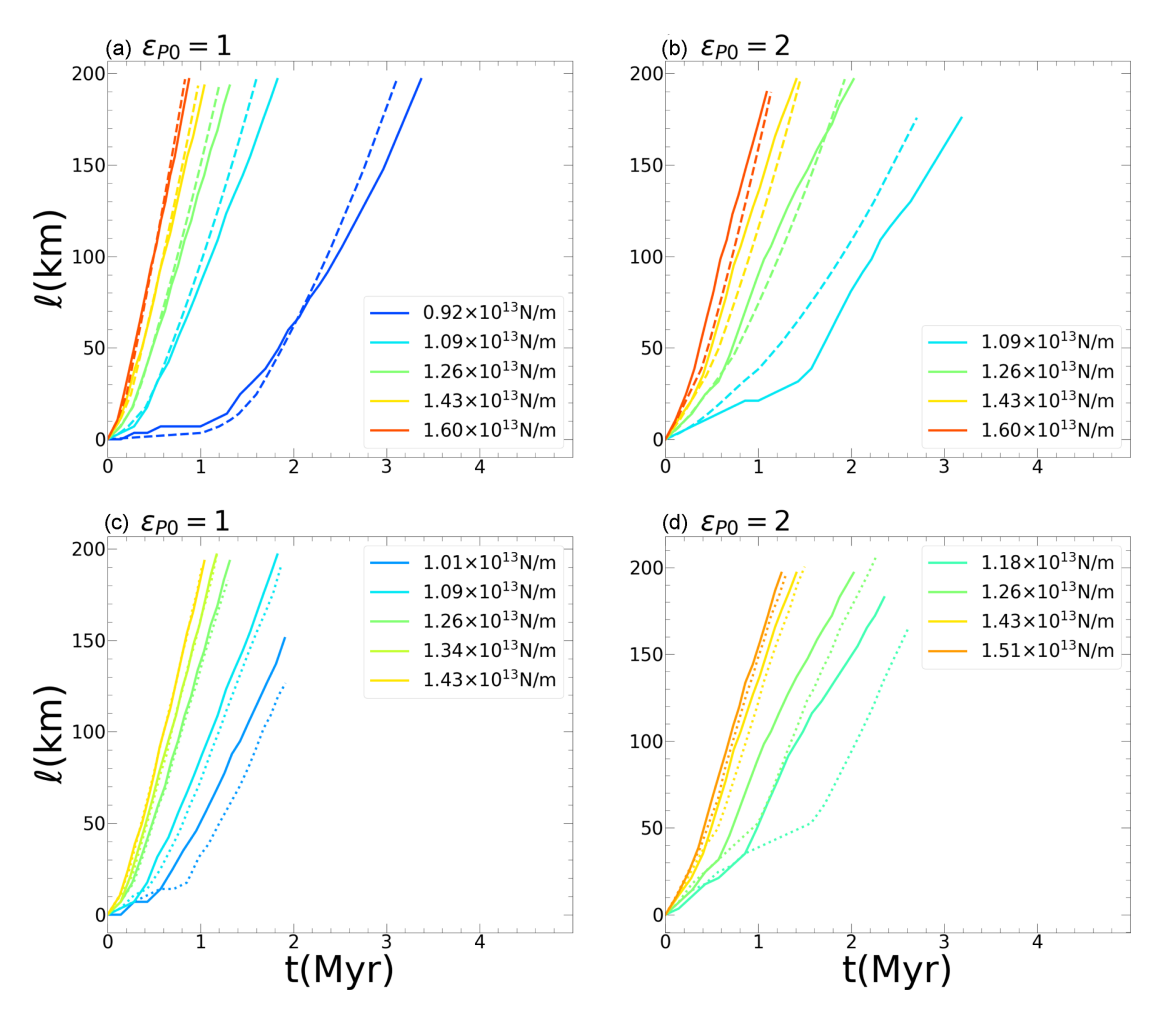


Figure 6. Plate displacement  $\ell$  versus time from force boundary condition with (a), (c)  $\varepsilon_{P0} = 1$  and (b), (d)  $\varepsilon_{P0} = 2$ . The colour represent applied force. Panels (a), (b) comparison between analytical solution (dashed) and numerical model (solid) with viscoplastic rheology. Panels (c), (d) the comparison between viscoplastic (solid) and viscoelasto-plastic model (dotted).

## 4.2 Force boundary

We now turn to the case where a force boundary is used. The dynamics of a nascent boundary evolves with the primary features in viscosity (Figs S1a-c) being similar to when velocity boundary conditions are used. A relatively high asthenospheric viscosity is used ( $\sim 10^{20} \text{ Pa} \cdot \text{s}$ ) allowing reasonable plate velocities with a relatively short plate length. The small domain is a reflection of the need to systematically sweep through the parameter range at a reasonable computational cost, and with the relatively large asthenospheric viscosity  $\eta_a \approx 10^{20}~\text{Pa}\cdot\text{s}$  acting on the short plate ( $\sim$ 400 km), the total  $F_a$  is equivalent to the plate with realistic length scale ( $L_P = 4000$  km) and viscosity ( $\eta_a = 10^{19}$  Pa·s). In the force boundary scenario, the plate interior stresses (Figs S1d-f) remain in compression, unlike the velocity boundary ones where the plate stress experiences a rapid conversion from compression to extension. The evolutionary pathway branches in two directions: For small applied forces the plate boundary remains stable and subduction never initiates, while for forces that exceed the threshold  $F_{xx} > T_S + F_I + T_S + T_S$  $N_{\rm HZ}$  (when u > 0 in eq. 15), subduction initiates. Displacement accelerates with time for a variety of applied forces and weakening rates, with close agreement between the finite element and analytical solutions (eqs 16 and 17; Fig. 6). The parameters used in the analytical solution see Table 1. Despite most of the parameters for the force boundary being the same as the ones used in the velocity boundary model, several differ. The  $K_1$  term governs the resistance associated with plate velocity, and is dominated by  $F_a$ , that is  $K_1 \approx \eta_a \frac{L_P}{d_a}$ . Although we set pre-factor for the viscosity law in the mantle to a higher value in the force boundary models, the effective viscosity does decrease with the non-linearity as plate velocity increases. Therefore, unlike the velocity boundary model with a constant  $K_1 = 4.4 \times 10^{20} \text{ Pa} \cdot \text{s}$ , the force boundary has two stages: prior to the plate boundary being fully weakened ( $\ell < \delta \varepsilon_{P0}$ ),  $K_1 = 2.6 \times 10^{21} \text{ Pa} \cdot \text{s}$  and after the weakening with a higher plate velocity and lower  $\eta_a$ ,  $K_2 = 1.9 \times 10^{21} \text{ Pa} \cdot \text{s}$ .

## 4.3 Plate curvature

Plate curvature, k, is a key factor in evaluating plate bending. In a bending plate, the strain rate is  $\dot{\varepsilon}_{ss} = -zu\frac{dk}{ds}$  (Buffet 2006), and the stress  $\sigma_{ss} = -4\eta zu\frac{dk}{ds}$ , so that plate curvature directly reflects plate deformation due to bending. Details on the measurement of plate curvature is

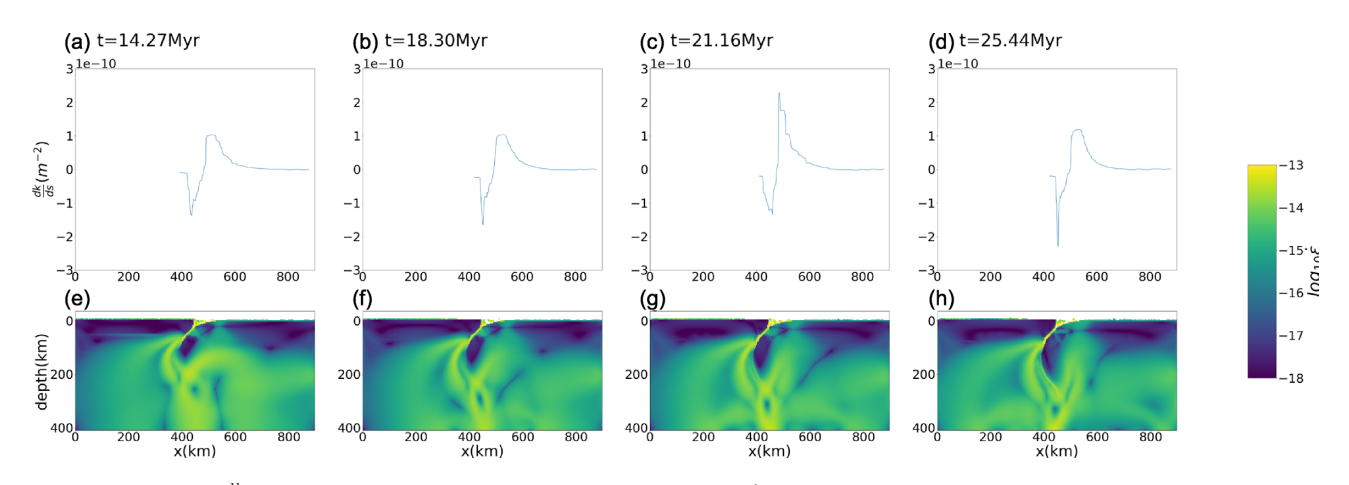
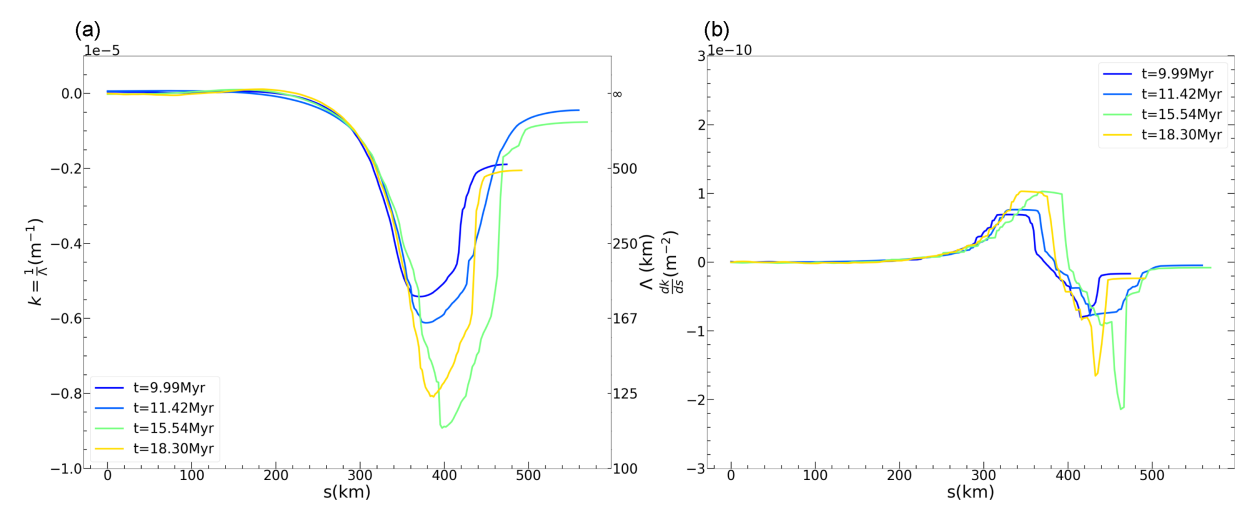


Figure 7. Panels (a)—(d)  $\frac{dk}{ds}$  versus x from velocity boundary model with u=1 cm yr<sup>-1</sup> at four different times. Panels (e)—(h) strain rate [as  $\log_{10}(\dot{\varepsilon})$ ] at the same time as (a)—(d). Peaks and troughs in (a)—(d) correlate with the hinge zone areas in (e)—(h).



**Figure 8.** Panels (a)  $\frac{dk}{ds}$  and (b) k versus s at different times from velocity boundary condition models with u = 1 cm yr<sup>-1</sup>. s is the distance from the right-hand end of the plate.  $\Lambda$  (on the right-hand axis of b) is the radius of the curvature, so that  $\Lambda = \frac{1}{k}$ .

provided in Supporting Information section S3. A comparison of  $\frac{dk}{ds}$  with maps of second invariant in strain rate from a case with u=1 cm yr<sup>-1</sup> (Fig. 7), shows two plateaus of  $\frac{dk}{ds}$ , one positive and one negative, that correlate with two yielding area (bending and unbending) in the hinge zone, where the  $\dot{e}_{II}$  is 2 orders of magnitude higher than in other regions. The spatial correlation between areas of high strain rate and the  $\frac{dk}{ds}$  peaks verifies the relation between strain rate and curvature. In previous studies, including Buffet (2006), the plate bending force is simplified as  $\Delta N = -\frac{1}{6}(\frac{H}{\Lambda_{\min}})^3 \eta u$ , based upon the assumption that k linearly increases from 0 to  $\frac{1}{\Lambda_{\min}}$ , and then linearly decreasing from  $\frac{1}{\Lambda_{\min}}$  to 0 with the same rate. This assumption has k changing with s linearly and symmetrically, and  $\frac{dk}{ds}$  is similar to a single period of a square-wave-like function in terms of s. The measured  $\frac{dk}{ds}$  versus s (Fig. 8b) shows negative and positive plateaus of  $\frac{dk}{ds}$  with roughly the same amplitudes validating the simple assumption. The symmetrical shape of k agrees with measurement in earlier studies (Capitanio et al. 2009; Farrington et al. 2014). This behaviour of  $\frac{dk}{ds}$  reflects symmetry of the bending and unbending of the plate. The maximum slab curvature is about 5–8  $\times$  10<sup>-6</sup> m<sup>-1</sup> (Fig. 8a), so that the minimum radius of curvature,  $\Lambda_{\min} = \frac{1}{k_{\max}}$ , is 100–200 km. Although k with s is linear and symmetric, the relationship  $\Delta N = -\frac{1}{6}(\frac{H}{\Lambda_{\min}})^3 \eta u$  may not apply as  $\eta$  is spatially heterogeneous due to plastic yielding, a point examined in the next section.

## 4.4 Hinge zone

A prominent feature of the hinge zone is the reduction in viscosity there (Figs 3 and S1), specially where the subducting slab experience substantial bending with a reduction in viscosity due to plastic yielding. In the hinge zone, there are typically two symmetric sectors with large deformation. The upper sector is typically in extension while the lower sector is in compression. Positive and negative peaks of  $\frac{dk}{ds}$  correlate with where the plate bends and unbends (Fig. 7). With the previously assumed constant slab viscosity, the resistance from plate bending is proportional to plate velocity  $\Delta N_b = K_b u$ , while when the hinge zone yields by plastic failure, the bending torque is independent of plate velocity. The analytical solution,  $N_{\rm HZ} = \frac{1}{6} H^2 S_{\rm HZ} \tau_y(\frac{dk}{ds})_{\rm max}$ , and measurement in numerical model (Fig. 5c) consistently predicts  $N_{\rm HZ} \approx 2 \times 10^{12} \, {\rm N} \, {\rm m}^{-1}$ . For the numerical models, the bending resistance is derived from  ${\rm d}N_b = k {\rm d}M$ , where M is bending moment.  $N_b$  only

changes substantially near the bending area, 450 < x < 550 km, and the total bending resistance across the hinge zone is  $\Delta N_b = N_b(450) - N_b(550)$ .  $\Delta N_b$  is independent of plate velocity u (Fig. S2a), agreeing with a bending torque in the hinge zone(s),  $N_{\rm HZ}$ , that remains constant. This result, in contrast to  $\Delta N_b$  being proportional to u with a constant  $\eta$ , reflects the dominance of plasticity within the hinge zone. With an increased plate velocity and higher strain rates, assuming plate curvature remains invariant, the hinge zone viscosity is reduced. The influence of plastic yielding on effective viscosity is quantified with an average viscosity in an analogous way a bending moment is defined (e.g. a weighting over  $\dot{\varepsilon} \times z$ )

$$\bar{\eta} = \frac{\int_{-H/2}^{H/2} \eta z^2 dz}{\int_{-H/2}^{H/2} z^2 dz} = \frac{12}{H^3} \int_{-H/2}^{H/2} \eta z^2 dz. \tag{22}$$

This then leads to the compact expression for  $M=-\frac{1}{3}\bar{\eta}uH^3\frac{\mathrm{d}k}{\mathrm{d}s}$ . On the other hand, due to plastic yielding,  $M=\frac{\tau_yH^2}{4}$ , a constant independent on u, we expect  $\bar{\eta}\sim\frac{1}{u}$ . For the quantity  $\bar{\eta}$  with s (shown with a log scale in Fig. S2b), the most prominent features are the dips, one between x=500 and 600 km and the other between x=400 and 500 km where  $\bar{\eta}$  varies by 2 orders of magnitude. These two low  $\bar{\eta}$  areas are the hinge zone areas where the strongest bending and unbending happens due to the plate yielding. In the hinge zones, the  $\bar{\eta}$  decrease with increased u, and the product of  $\bar{\eta}$  and u remain generally constant as u changes (Fig. S2c), verifies that the reduction of  $\bar{\eta}$  due to plastic yielding cancels the variation of strain rate due to varied plate velocity and the bending torque is generally independent of u.

#### 4.5 Initiation time

Plate stress and plate motion evolve in velocity-imposed and force-imposed scenarios, with the principal driving force experiencing a transition from an initial external compression to dominance by slab pull. Consequently, we define an initiation time when slab pull becomes dominant. For velocity boundary models,  $F_{xx}$  decreases with time, and we define the time when  $F_{xx} = 0$  to be the time of initiation,  $t_{SI}$ . After  $t_{SI}$ , the internal driving force (negative buoyancy), is able to overcome all the resistance and the plate can move without any external driving force. From eq. (14) we obtain  $\ell_{SI} = (D + (\eta \frac{L_P}{d_a} + K_b)u_0 + N_{HZ} + F_I)/(\Delta\rho \sin\theta)$ . Initially, the thermal contraction is the major source for negative buoyancy as no metamorphism takes place. At  $\ell \approx 150$  km, the density anomaly from eclogite metamorphism augments the negative buoyancy (Fig. 4). As plate convergence reaches about 200 km,  $F_{xx}$  becomes less than zero, and with the inclusion of eclogite metamorphism, we obtain  $\ell_{SI} = (D + (\eta \frac{L_P}{d_a} + K_b)u_0 + N_{HZ} + F_I + d_c\Delta\rho_e g\sin\theta \times (150 \text{ km}))/(\frac{1}{2}H\rho_0\alpha\Delta Tg\sin\theta + d_c\Delta\rho_e g\sin\theta)$ . As  $t_{SI} = \frac{\ell_{SI}}{u}$ , we see that that this timescale is primarily influenced by plate velocity, and secondarily plate age and plate strength through the bending toque and isostatic force (Figs 9a–c). The increase of  $\epsilon_{P0}$  slows the weakening, thereby delaying the onset of a state of neutral stress.

Unlike the velocity boundary where the  $F_{xx}$  changes with time, for the constant force boundary, as the plate interior stress is governed by the boundary condition,  $F_{xx}$  equals the applied boundary force. Together with the accumulation of negative buoyancy and weakening, the plate speed u accelerates with time. Therefore, we define the initiation time as the time when the plate convergence reaches a certain quantity  $\ell_{SI}$ . With eq. (23)

$$t_{SI} \approx \frac{4K_1\tau_{y0}}{B_1^2 + 4C(F_{xx} - A - F_{I} - N_{HZ})} + \frac{K_1(\ell_{SI} - \delta\varepsilon_{P0})}{F_{xx} - D - F_{I} - N_{HZ}}.$$
 (23)

The exact solution of  $t_{\rm SI}$ , see eq. (S3). Here we choose  $\ell_{\rm SI}=200$  km, roughly equal to the  $\ell_{\rm SI}$  for velocity boundary models. Maps show the prediction of the initiation time from eq. (S3), with force, plate age,  $\tau_{\rm max}$  and  $\varepsilon_{P0}$  (Figs 9d–f). Due to the nature of the force boundary condition, the plate experience continuous speedup, and together with the increasing negative buoyancy, the  $t_{\rm SI}$  is relatively small compared to the velocity boundary models where the plate velocity is confined with the boundary condition. Despite of the absolute  $t_{\rm SI}$ , the changing of  $t_{\rm SI}$  with respect to the plate age,  $\tau_{\rm max}$  and  $\varepsilon_{P0}$  obey the same trend as found for velocity models (Figs 9a–c). The No SI domains (the shaded regions in Figs 9d–f) predicted from eq. (S3) are consistent with the numerical models, that is when an insufficient force applied to the boundary fails to induce subduction initiation.

## 4.6 Work done to initiate subduction

Having established the time to initiate subduction, we can now turn to the total work done by the compression up to this time. In the imposed velocity configuration, the in-plate force is integrated with plate convergence

$$W(\ell) = \int_0^\ell F_{xx}(\ell') d\ell'$$
 (24)

in which W reflects the work done on the system by the boundary condition. Initially, W increases with  $\ell$  as  $F_{xx}$  is compressional and the plate motion is driven by boundary velocity (Fig. S4). However, as negative buoyancy accumulates and the plate boundary weakens, W eventually peaks when  $F_{xx} = 0$ , the same criteria defining  $t_{SI}$ . Consequently, at the peak of  $W(\ell)$ , we define  $W_{SI}$ , the total work done to initiate subduction. As expected, we find a close agreement between the work predicted by the simple force balance model with the full numerical results for the same rate of weakening, controlled through  $\varepsilon_{P0} = 1$  (Fig. 10a). On average, the simple model slightly overpredicts the work done as a function of convergence velocity.

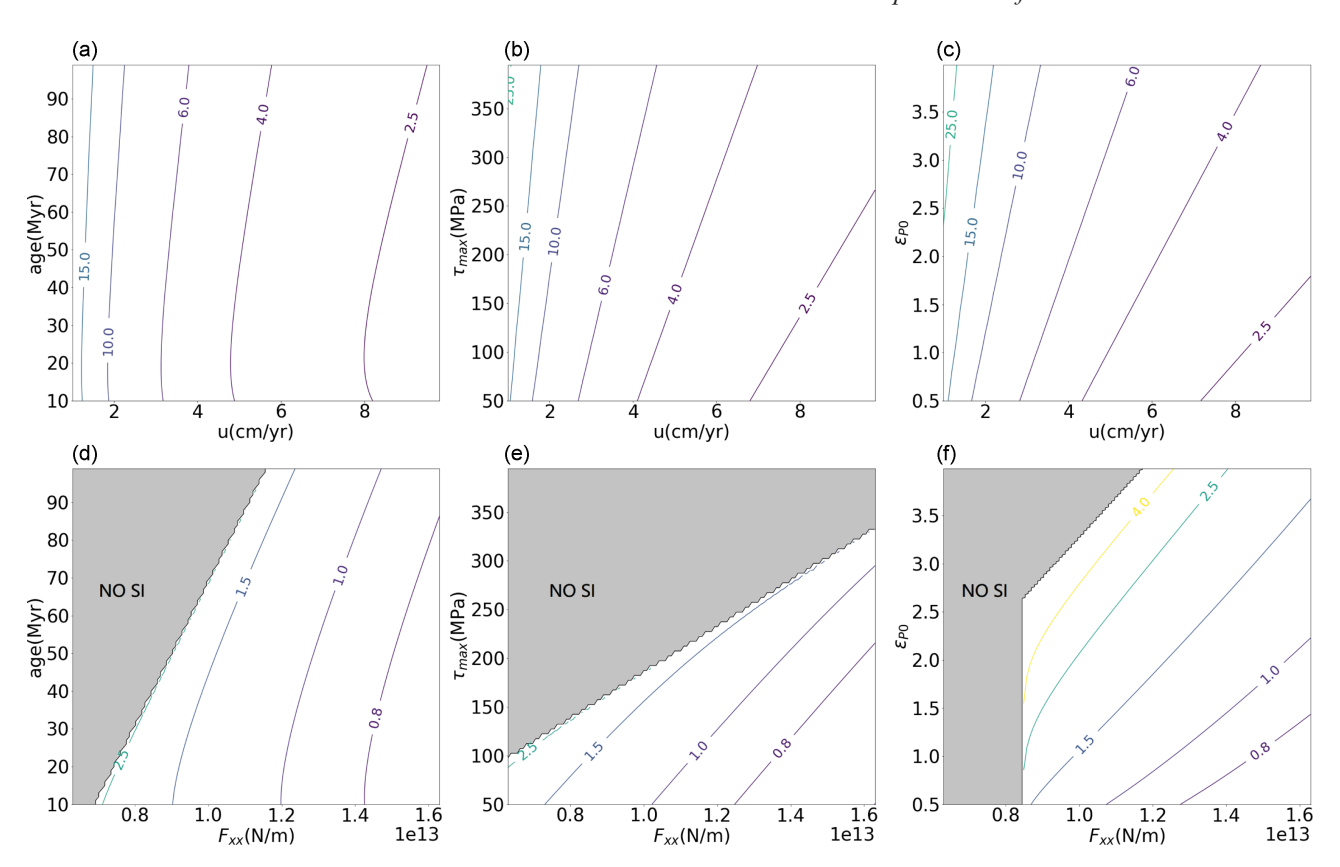


Figure 9. (a)–(c) Contours of  $t_{\rm SI}$  from analytical solution for velocity boundary models. (d)–(f) The same contours for the force boundary models. The varying parameter include plate velocity u for velocity boundary models and boundary force  $F_{xx}$  for force boundary models. The age of subduction plate (a, d), plate strength  $\tau_{\rm max}$  (b, e) and weakening rate  $\varepsilon_{P0}$  (c, f) are varied. The grey area in (d)–(f) denotes parameter domains where there is no initiation. When the parameters are not varied, the default values are plate age = 40 Myr,  $\tau_{\rm max} = 150$  MPa,  $\varepsilon_{P0} = 1$ .

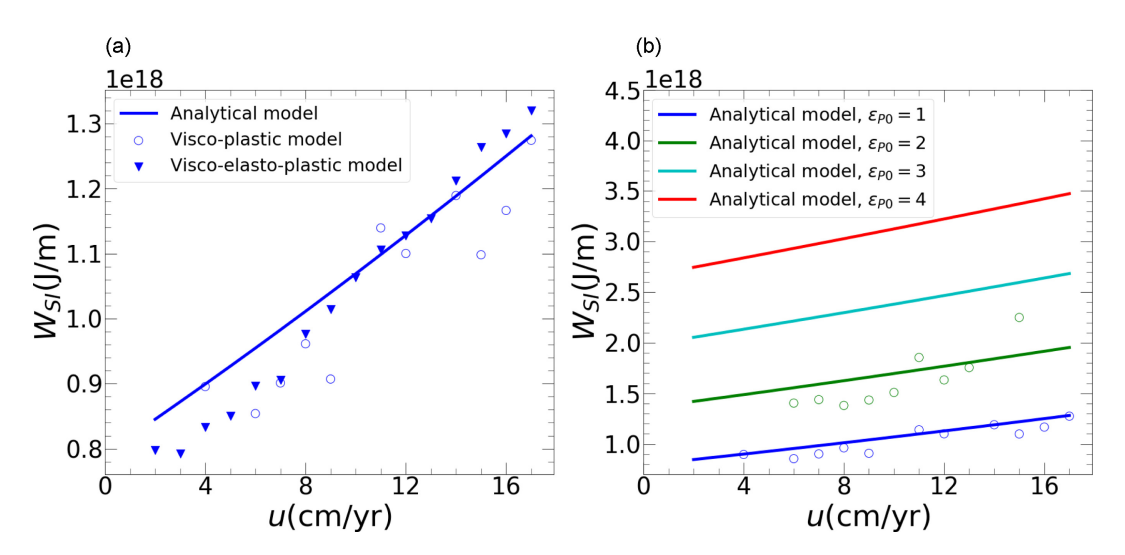


Figure 10. (a) The work done to initiate subduction,  $W_{SI}$ , from models with different convergent velocities at  $\varepsilon_{P0} = 1$ . Solid line is for analytical solutions, open circles for viscoplastic models, and filled triangles for viscoplastic models. (b) Analytical prediction of  $W_{SI}$  vs u with different  $\varepsilon_{P0}$ 's (colour-coded) for viscoplastic rheologies.

As an increased convergent velocity u incurs greater dissipation in the system, the numerical models and analytical models consistently predict an increase of  $W_{SI}$  with larger u (Fig. 10a). In addition to the plate velocity u, the dissipation is strongly influenced by the weakening process, therefore we evaluate the  $W_{SI}$ -u with different weakening rate from the analytical solution using eqs (14) and (24) (Fig 10b). With an increase in u from 1 to 10 cm yr<sup>-1</sup>,  $W_{SI}$  only increases by less than  $5 \times 10^{17}$  J m<sup>-1</sup>, while an increase of  $\varepsilon_{P0}$  by a step of 1 can lead to  $1 \times 10^{18}$  J m<sup>-1</sup> increase in  $W_{SI}$ . Compared to plate velocity, the plate weakening caused by the plate motion has a larger impact on the total

energy dissipation in the system and demonstrates the importance of the rate of subduction zone nucleation in determining how hard, or how much work it takes, to make a new subduction zone.

#### 4.7 Isostatic force

The isostatic force  $F_1$ , defined in eq. (11), is the normal force due to lateral pressure gradients across the plate boundary where the plate's thermal and compositional structure change sharply. The integration of pressure over depth with respect to x,  $F_p = \int_0^H p dz$ , across the plate boundary in the numerical model shows large fluctuations due to plate bending and interplate friction, but with a clear offset between overriding and subducting plates (Fig. S3). Analytically, the estimated combination of thermal and compositional isostatic forces,  $F_1$  (eqs 9 and 10), is  $2.07 \times 10^{12} \text{ N m}^{-1}$ , close to the measured difference across the plate boundary (Fig. S3). In different scenarios of subduction initiation,  $F_1$  can function as either a driving or resistance term. In the model, the subduction initiation is induced by a horizontal driving force, and  $F_1$  pushes against the far-field driving forces and resists plate motion, hence inhibits subduction initiation. In the other mode of subduction initiation, so called spontaneous subduction initiation (Stern 2004), the slab founders vertically into the mantle without external compression, and  $F_1$  acts as a force that drives local compression against plate bending (Nikolaeva *et al.* 2010; Leng & Gurnis 2015). In our cases, an  $F_1$  of  $\approx 2 \times 10^{12} \text{ N m}^{-1}$  is roughly equal to the estimated bending torque but smaller than the initial plate boundary friction; consequently  $F_1$  is insufficient to overcome the resisting forces and no spontaneous subduction initiation occurs in the model, consistent with the finite elements computations.

## 4.8 Elasticity

Thus far, the calculations have been based on a fluid constitutive relation, but the lithosphere experiences elastic deformation, which can be bridged with viscoelastic models. Here we compare viscoplastic results with ones with viscoelasticity to isolate the role of elasticity during subduction initiation. This is important because both constitutive relations have been used in prior studies, including those using viscoelasto–plastic (Toth & Gurnis 1998; Gurnis *et al.* 2004; Nikolaeva *et al.* 2010; Leng & Gurnis 2015) and those assuming viscoplastic (Zhou *et al.* 2018; Arcay *et al.* 2020; Maunder *et a*<sub>1</sub>. 2020). We assume the material deforms as a Maxwell body, with a shear modulus  $\mu$ ,  $\dot{\varepsilon} = \dot{\varepsilon}_e + \dot{\varepsilon}_v = \frac{\dot{\tau}}{2\mu} + \frac{\tau}{2\eta}$  which has a relaxation time  $t_e = \frac{\eta}{\mu}$  (Ranalli 1995). For a lithosphere with  $\eta = 10^{24}$  Pa · s (Fig. S2) and  $\mu = 3 \times 10^{10}$  Pa,  $t_e \approx 1$  Myr, on the same order as subduction initiation. However, with the presence of plasticity, the effective viscosity can drop by orders of magnitude within the hinge zone after the nucleation stage, when the plate bending becomes more fully developed and the interplate boundary weakens. With a hinge zone viscosity  $\approx 10^{23}$  Pa · s,  $t_e \approx 0.1$  Myr, smaller than the timescale for subduction initiation. This suggests that elasticity is likely to diminish as plastic yielding comes to dominate.

The role of elasticity is examined by recalculating models presented earlier, while keeping all parameters the same except substituting a viscous with a Maxwell body (Moresi *et al.* 2003). From the relation  $F_{ss}$  versus  $\ell$  (Fig. 4c), we observe how elasticity changes the stress evolution. With viscoelasticity, the force starts at 0 and increases with convergence as elastic stresses buildup. Later, as the plate bends and the hinge zone yields, the relaxation time drops by orders of magnitude, and the governing rheology turns from viscoelastic to dominantly viscous. The drop of  $\eta_{eff}$  and  $t_e$  weakens the role of elasticity, and the evolution of the viscoelasto–plastic model closely follows the viscoplastic model after the elastic stress buildup stage (Fig. 4d). The work done by the compression to initiate subduction,  $W_{SI}$ , is computed for the viscoelasto–plastic cases as for the viscoplastic ones. Although the pattern of  $W_{SI}$  versus  $\ell$  is not strongly influenced by the elasticity (Fig. 10a), viscoelasto–plastic models have systematically higher  $W_{SI}$  when u is large (u > 10 cm yr<sup>-1</sup>). With small u, as the timescale of subduction initiation is much greater than the Maxwell relaxation time, the viscous deformation dominantly governs the viscoelastic system and the role of elasticity is negligible. In contrast, with a sufficiently large u, the time scale of subduction initiation becomes smaller than the Maxwell time, allowing the elasticity to play a larger role. Care must be taken with the elastic time steps  $\Delta t_e$  in the numerical model, which can influence the stress evolution, as discussed in the Supporting Information. With an appropriately small  $\Delta t_e$  [a domain where viscoelastic benchmarks show that Underworld solutions converge to analytical ones (Moresi *et al.* 2003; Farrington *et al.* 2014)], the computations show that the role of elasticity can be minor (Fig. 4c).

When force boundary conditions are used there are also some differences between models with and without elasticity. With elasticity, the amount of convergence rate slows with time and is associated with a systematic increase in the resisting force due to the addition of elasticity (Figs 6c–d). The difference caused by elasticity is minor for cases with large  $F_{xx}$ . A larger force leads to more yielding and a smaller relaxation time. For a smaller  $F_{xx}$ , the elasticity makes a larger difference, as the initiation process occurs over a timescale that is comparable to the Maxwell time.

The addition of elasticity provides an additional force after bending becomes developed, with the elastic stress adding an additional resistance force which slows the incoming plate. However, elasticity does not cause a substantial difference in most cases due to plasticity, which we verify by varying the yielding stress  $\tau_{\text{max}}$  in velocity boundary models (Fig. S6) and force boundary models (Fig. S7). With velocity boundary conditions and a low yield stress (150–300 MPa, Figs S6a and b) the hinge zone deformation is dominated by plastic yielding, and the viscoelasto–plastic and viscoplastic models produce nearly indistinguishable  $F_{xx} \sim \ell$  curves. When yield stress increases (600 MPa to 1.2 GPa), the hinge zone viscosity is less affected by the yielding, and the elasticity causes a more prominent difference (Fig. S6) when the subduction zone is fully developed ( $\ell \approx 300$  km). For the force boundary model (Fig. S7), the difference in  $\ell \sim t$  due to elasticity is distinct

only when the applied force is small, and the increased yield stress (300 MPa, Fig. S7b) makes the elasticity more prominent. The diminished role of elasticity with decreased yield stress confirms the influence of elasticity is governed by plastic yielding: With a small yield stress ( $\tau_{max}$  = 150–300 MPa), the role of elasticity during subduction initiation seems limited.

## 5 DISCUSSION

We have developed a simple, time-dependent analytical model tailored to induced subduction initiation with two different boundary conditions—velocity and force—corresponding to different tectonic settings. With velocity boundary conditions, plate motion is regulated by the boundary conditions regardless of the state of stress, and such a scenario would reflect subduction initiation localized along a small segment of strike of a nascent plate boundary. As the nascent segment is small, the resistance against plate motion from subduction initiation is similarly small compared to the far-field forces driving convergence; consequently, the plate motion is mostly unaffected by the abrupt changes of resistance during initiation, thereby maintaining a constant velocity. The Puysegur subduction zone south of New Zealand (Collot *et al.* 1995; Gurnis *et al.* 2019; Shuck *et al.* 2021) is in such a state. Here, the Australian Plate subducts under the Pacific Plate over a lateral extent of  $\approx$ 400 km, small compared to the more fully developed subduction zones over thousands of kilometre pulling Australia to the north. In this example, the Australia–Pacific Plate kinematics are not expected to experience a substantial change due to the Puysegur subduction initiation which started at  $\approx$ 15 Ma (Lebrun *et al.* 2003; Sutherland *et al.* 2006; Shuck *et al.* 2022) and the model developed here is applicable to this setting.

In contrast, the force boundary reflects the extreme where the plate kinematics are initially governed by the applied far-field stress, but as the initiated boundary grows it can cause a change in plate kinematics. The reorganization of Pacific Plate motion at ≈50 Ma inferred from the Hawaiian-Emperor seamount Bend (HEB), and global plate circuits (Muller et al. 2016; Torsvik et al. 2017), serves as an example of changing plate kinematics that could be influenced by subduction initiation. The initiation of subduction zones in the western and southwest Pacific at around 50 Ma, including Izu-Bonin-Mariana (Reagan et al. 2019) and Tonga-Kermadec (Sutherland et al. 2020), is the potential cause for the rearrangement of Pacific Plate motion. The hypothesis that IBM initiation causes a change in Pacific Plate motion is widely discussed and is based on the view that IBM initiated spontaneously (Stern & Bloomer 1992; Reagan et al. 2019). However, it takes time for sufficient driving force to accumulate in the upper mantle and this time has to be larger than  $t_{SI}$  derived here. The quantity  $t_{SI}$  reflects the time when the forces local to a subduction zone have switched from resisting to driving but plate motion will be a function of both downdip slab length and along strike distance of a subduction zone. These were addressed in fully dynamic global calculations (Hu et al. 2022). Those calculations show that the initiation of the Izu-Bonin-Mariana subduction zone is insufficient for Pacific Plate rearrangement at 50 Ma. However, by 47 Ma, the IBM slab would have a downdip length of 400 km (using the estimate of Reagan et al. (2019) for forearc extension as a proxy for convergence), considerably larger than the ≈200 km we find here for the transition from forced to self-sustaining subduction. Hu et al. (2022) found that the total change in Pacific Plate direction from IBM initiation would be about 10°. The HEB angle by itself reflects about 60° change, but about half of of this is likely due to the rapid motion of the Hawaiian plume to the south between 80 and 50 Ma (Tarduno et al. 2003). Instead of just IBM initiation, Hu et al. (2022) propose the demise of Kronotsky subduction zone in the north Pacific is the key factor, and IBM a secondary factor, leading to the rearrangement of Pacific Plate motion in the Eocene. IBM is an example of the setting described by the models with the force boundary conditions.

The viscosity of the asthenosphere can play a role in resisting subduction initiation. In the model with imposed velocity boundary conditions, the effective viscosity at the base of lithosphere is  $10^{19}-10^{20}$  Pa·s. The asthenospheric viscosity is governed by the non-Newtonian flow, eq. (18), and agrees with an estimate of viscosity in the asthenosphere beneath the Indian Plate from post-seismic relaxation (Hu et al. 2016).  $F_a$  is estimated to be  $10^{11}-10^{12}$  N m<sup>-1</sup> with several cm yr<sup>-1</sup> plate motion. For the force boundary models, with a relatively large asthenospheric viscosity ( $\eta_a \approx 10^{20}$  Pa· s), the total shear force is  $F_a \approx 10^{12}$  N m<sup>-1</sup>. From the force boundary model, we obtain a good approximation of the resistance from asthenosphere for a plate with a much more realistic length scale (thousands of km). The resistance from the asthenosphere is a small but non-negligible component in the force balance.

Elasticity plays a role in subduction initiation. Viscoelastic rheologies have been widely applied in geodynamic models (Toth & Gurnis 1998; Moresi et al. 2003; Gurnis et al. 2004; Gerya et al. 2008; Capitanio et al. 2009; Marques et al. 2013; Farrington et al. 2014) to accommodate the long-term fluid flow and short-term elastic deformation. We compare the viscoplastic with equivalent viscoelasto—plastic models, and show that the presence of plasticity effectively reduces the Maxwell time, reducing the importance of elasticity during subduction initiation, but a conclusion dependent on the yield stress. With larger yield stresses elasticity becomes more important and stores energy that contributes to resistance against bending, as in the models of Farrington et al. (2014) where a strong (non-plastic) layer is embedded within the core of the slab. When the yield stress is small, yielding occurs at the edges of the slab, the viscoelasto—plastic models are not distinguishable from viscoplastic ones in terms of either stress or strain. Although there has long been evidence for deformation within the outer portions of the bending slab through seismicity and normal faulting within the trench (Watts 2001) and in some numerical models (Capitanio et al. 2007, 2009; Farrington et al. 2014) a strong core embedded in the slab is assumed to account for the temperature dependent viscosity and low strain rate in the centre of a bending plate, there is also evidence that the core of the slab might be weak. Relatively small yield stresses within the core of slab is supported by plate rigidities that drop by more than 3 orders of magnitude near the trench (Billen & Gurnis 2005). Large earthquakes (with moment magnitude 8 or larger) can rupture a substantial part of the lithosphere near the hinge zone (Kikuchi & Kanamori 1995), suggesting that there could be little elastic strength of the bending plate. However, the arguments in Kikuchi & Kanamori (1995) and

Billen & Gurnis (2005) follow from measurements made in fully developed subduction zones and we currently do not have direct evidence on the strength of the incoming plate in nascent subduction settings. Overall, the elasticity provides an extra resistance against subduction initiation especially during the nucleation stage, and slows plate motion, but elasticity does not appear to be a first order factor governing the time to initiate or the total work done to initiate subduction.

From geophysical observations offshore and from the geological on- and offshore, two modes of subduction initiation are inferred: Spontaneous and induced (Gurnis et al. 2004; Stern 2004; Arculus et al. 2015; Sutherland et al. 2017; Guilmette et al. 2018; Reagan et al. 2019; Shuck et al. 2022). With the spontaneous initiation scenario, the plate is pulled downward (bent) spontaneously without a strong far-field compression (that is  $F_{xx} \approx 0$  in our formulation); in other words, the local buoyancy forces within the nascent plate boundary are sufficient to over come the resisting forces. Interpretation of the IBM forearc (Stern & Bloomer 1992; Reagan et al. 2019) and computational models (Dymkova & Gerya 2013; Leng & Gurnis 2015; Stern & Gerya 2018; Maunder et al. 2020) suggest that over-riding plate extension and rapid trench roll back are prominent outcomes of spontaneous subduction initiation. Our numerical models with the full solution of the coupled non-linear system never produced spontaneous initiation; in the force boundary model, a small  $F_{xx}$  results in a stable plate boundary while a large  $F_{xx}$  results in an induced mode of subduction initiation in which the slab is coupled with the overriding plate during the subduction. In the analytical model, for spontaneous initiation ( $F_{xx} = 0$ ), the only possible driving force would be  $F_1$ . We note that  $F_1$  in eq. (1) is treated as a resistant force as it is a horizontal compression pushing against the incoming plate (and the computational models support this assumption). However, for the spontaneous initiation scenario, the future subducting plate is not moving forward and consequently F<sub>1</sub> acts as a local compression which could initiate subduction. If we make this assumption, then a criteria for spontaneous initiation is  $F_1 > \Delta N_b$ . Numerically, we estimate a typical bending force to be  $\sim 2 \times 10^{12}$  N m<sup>-1</sup> (Fig. S2a). This is close to that from the analytical model where we estimate the bending torque across the hinge zone, eq. (5), to be  $1.8 \times 10^{12}$  N m<sup>-1</sup> (with  $s_{\rm HZ} \approx 100$  km, H = 60 km,  $(dk/dz)_{\rm max} \approx 10^{-10} {\rm m}^{-2}$  and  $\tau_{\rm max} =$ 300 MPa). The computational and analytical results both show  $\Delta N_b$  to be  $2 \times 10^{12}$  N m<sup>-1</sup>, roughly equal to  $F_1$  ( $\approx 2 \times 10^{12}$  N m<sup>-1</sup>), so the condition for spontaneous subduction initiation is only marginally possible with the model setup. However, with other sources of resistance from plate boundary friction and asthenospheric shear that would need to occur when the new shear zone forms, the observation that we never observe spontaneous initiation in our full non-linear computations is consistent with the analytical model. This theoretical result is also consistent with the models of Zhou & Wada (2021) who argued that models with induced versus spontaneous initiation better explained the thermal history of the metamorphic soles of ophiolites.

With the half space cooling model, H is proportional to (plate age)<sup>1/2</sup>, so that the thermal isostatic force  $F_{\text{thermal}} \sim H^2$ . Unlike previous work suggesting that plate rigidity, with constant viscosity, is proportional to  $H^3$ , we show that with plastic yielding, plate bending resistance is proportional to  $H^2$ . Together these indicate that the scaling of  $F_{\rm I}$  and  $\Delta N_{\rm b}$  with subducting plate thickness is of the same order, so that the subducting plate age might not be a determining factor for subduction initiation. Both young and old plates have a chance to initiate subduction, in agreement with the computational models of Arcay *et al.* (2020). Two sites of Cenozoic subduction initiation are IBM and the Matthews–Hunter (Patriat *et al.* 2015, 2019) which initiated with widely different subduction plate ages: 70 Myr old for IBM (Hall *et al.* 2003) and about 20 Myr for Matthews–Hunter using the reconstructions in Seton *et al.* (2016). Evidence from some ophiolites have suggested very young ages for the age of plates during subduction initiation (van Hinsbergen *et al.* 2015; Maffione *et al.* 2015).

Despite the absence of spontaneous initiation in the full numerical models, we suggest that several conditions could lead to this possibility. First, a buoyant overriding plate, either through its composition or with a young thermal age, which is able to produce a large  $F_{\rm I}$ . An even weaker subducting plate, with a low  $\tau_{\rm max}$  can essentially reduce the plate bending force, and may lead to a propensity of spontaneous initiation. In principle, an even weaker plate boundary, for example a weak interplate friction  $T_{\rm s}$ , might allow subduction to unfold spontaneously.

Another means to initiate subduction is through a vertical force during subduction propagation. One potential source of the additional vertical force is the shear force from the along-strike propagation of subduction associated with the 3-D 'unzipping' behavior of a subduction zone (Maunder *et al.* 2020). In contrast to the free slip boundary widely used in computational models, models with open boundaries at their base (Zhou *et al.* 2018; Arcay *et al.* 2020) are more likely to produce spontaneous initiation.

The timescale for initiating a new subduction zone is a key outcome of the mechanical models and can be constrained with geological observations. By definition,  $t_{SI}$  describes the duration it takes for the local forces to exceed the external driving forces. When this change in the force balance occurs, we showed that the state of stress within the plate margins switches from compression to extension. Recently, detailed analysis of seismic images in the context of biostratigraphic ages from an existing borehole within the Solander Basin on the over-riding plate proximal to the Puysegur Trench (Patel *et al.* 2021; Shuck *et al.* 2021), demonstrated a transition from compression to extension between 15 and 5 Ma as the new subduction zone formed (Shuck *et al.* 2022). An initial burst of compression at 15 Ma is interpreted as the initial compression during subduction nucleation (Shuck *et al.* 2022), in close agreement with the well-constrained relative motion between the Australian and Pacific Plates (Sutherland *et al.* 2006; Gurnis *et al.* 2019). The transition from compression to extension is interpreted as the transition in the local force balance. This lead to a 10 Myr timescale for the initiation of the Puysegur subduction zone, although Shuck *et al.* (2022) also show that this transition is changing along strike and comparing these observations against models will require a 3-D domain. The dating of ophiolites provides another constraint on the timescale for subduction initiation (Hacker 1994). In Oman, the geochronological dating of the Semail ophiolite indicates that initial thrusting predates the upper plate extension by at least 8 Myr (Guilmette *et al.* 2018). These different observations independently indicate in evolving subduction zones, the time for the stress state to become neutral is  $\sim$ 10 Myr. This estimate matches the velocity boundary models with u = 2-4 cm yr<sup>-1</sup> (Figs 9a–c), but do not fall within the regime provided by the force boundary models (Figs 9d–f).

#### ACKNOWLEDGMENTS

The authors thank Fabio Capitanio and Ikuko Wada for detailed and insightful reviews which lead to improvements in the manuscript. This work is supported by the National Science Foundation through awards OCE-1654766, EAR-1645775 and OCE-2049086. The authors acknowledge the Texas Advanced Computing Center (TACC) at The University of Texas at Austin for providing HPC resources that have contributed to the research results reported within this paper.

#### DATA AVAILABILITY

The data and code underlying this paper are available in CaltechDATA, at https://doi.org/10.22002/D1.8958.

#### REFERENCES

- Arcay, D., Lallemand, S., Abecassis, S. & Garel, F., 2020. Can subduction initiation at a transform fault be spontaneous?, *Solid Earth*, **11**(1), 37–62.
- Arculus, R.J. et al., 2015. A record of spontaneous subduction initiation in the Izu-Bonin-Mariana arc, Nat. Geosci., 8, 728–733.
- Billen, M.I. & Gurnis, M., 2005. Constraints on subducting plate strength within the Kermadec Trench, J. geophys. Res, 110, doi:10.1029/2004JB003308.
- Buffet, B., 2006. Plate force due to bending at subduction zones, *J. geophys. Res.*, **111**(B9), 1–9.
- Capitanio, F., G Morra, G. & Goes, S., 2007. Dynamic models of downgoing plate-buoyancy driven subduction: Subduction motions and energy dissipation, *Earth planet. Sci. Lett.*, 262, 284–297.
- Capitanio, F.A., Morra, G. & Goes, S., 2009. Dynamics of plate bending at the trench and slab-plate coupling, *Geochem. Geophys. Geosyst.*, 10(4), doi:10.1029/2008GC002348.
- Collot, J.-Y., Lamerche, G., Wood, R.A., Delteil, J., Sosson, M., Lebrun, J.-F. & Coffin, M.F., 1995. Morphostructure of an incipient subduction zone along a transform plate boundary: Puysegur ridge and trench, *Geology*, 23, 519–522.
- Crameri, F. et al., 2012. A comparison of numerical surface topography calculations in geodynamic modelling: an evaluation of the 'sticky air' method, Geophys. J. Int., 189(1), 38–54.
- Dymkova, D. & Gerya, T., 2013. Porous fluid flow enables oceanic subduction initiation on Earth, *Geophys. Res. Lett.*, **40**(21), 5671–5676.
- Farrington, R., Moresi, L.-N. & Capitanio, F., 2014. The role of viscoelasticity in subducting plates, Geochem. Geophys. Geosyst, 15, 4291–4304.
- Gerya, T.V., Connolly, J. A.D. & Yuen, D.A., 2008. Why is terrestrial subduction one sided?, Geology, 36, 43–46.
- Guilmette, C. et al., 2018. Forced subduction initiation recorded in the sole and crust of the Semail Ophiolite of Oman, Nat. Geosci., 11(9), 688–695.
- Gurnis, M., Hall, C. & Lavier, L., 2004. Evolving force balance during incipient subduction, Geochem. Geophys. Geosyst., 5(Q07001), 1–31.
- Gurnis, M. et al., 2019. Incipient Subduction at the contact with stretched continental crust: the Puysegur Trench, Earth planet. Sci. Lett., 520, 212– 219.
- Hacker, B., Abers, G. & Peacock, S., 2003. Subduction factory 1. Theoretical mineralogy, densities, seismic wave speeds, and H<sub>2</sub>O contents, J. geophys. Res. 108(B1), doi:10.1029/2001JB001127.
- Hacker, B.R., 1994. Rapid emplacement of young oceanic lithosphere: argon geochronology of the Oman Ophiolite, *Science*, 265(5178), 1563–1565.
- Hall, C., Gurnis, M., Sdrolias, M., Lavier, L.L. & Müller, R.D., 2003. Catastrophic initiation of subduction following forced convergence across fracture zones, *Earth planet. Sci. Lett.*, 212, 15–30.
- Hu, J., Gurnis, M., Rudi, J., Stadler, G. & Müller, D., 2022. Dynamics of abrupt change in Pacific Plate motion around 50 Ma, *Nat. Geosci.*, 15, 74–78.
- Hu, Y., Bürgmann, R., Banerjee, P., Feng, L., Hill, E.M., Ito, T., Tabei, T. & Wang, K., 2016. Asthenosphere rheology inferred from observations of the 2012 Indian Ocean earthquake, *Nature*, 538(7625), 368–372.
- Kikuchi, K. & Kanamori, H., 1995. The Shikotan earthquake of {O}ctober 4, 1994: {L}ithospheric earthquake, *Geophys. Res. Lett.*, **22**, 1025–1028.
- Lebrun, J.-F., Lamarche, G. & Collot, J.-Y., 2003. Subduction initiation at a strike-slip plate boundary: the Cenozoic Pacific-Australian

- plate boundary, south of New Zealand, J. geophys. Res., 108(B9), doi:10.1029/2002JB002041.
- Leng, W. & Gurnis, M., 2011. Dynamics of subduction initiation with different evolutionary pathways, *Geochem. Geophys. Geosyst.*, 12, 1–16, doi:10.1029/2011GC003877.
- Leng, W. & Gurnis, M., 2015. Subduction initiation at relic arcs, Geophys. Res. Lett., 42, 7014–7021.
- Maffione, M., Thieulot, C., van Hinsbergen, D. J.J., Morris, A., Plümper, O.
  & Spakman, W., 2015. Dynamics of intraoceanic subduction initiation: 1.
  Oceanic detachment fault inversion and the formation of supra-subduction zone ophiolites, *Geochem. Geophys. Geosyst.*, 16(6), 1753–1770.
- Mansour, J. et al., 2020. Underworld2: Python geodynamics modelling for desktop, HPC and Cloud, J. Open Sourc. Softw., 5(47), doi:10.21105/joss.01797.
- Marques, F.O., Nikolaeva, K., Assumpção, M., Gerya, T.V., Bezerra, F.H., do Nascimento, A.F. & Ferreira, J.M., 2013. Testing the influence of farfield topographic forcing on subduction initiation at a passive margin, *Tectonophysics*, 608, 517–524.
- Maunder, B., Prytulak, J., Goes, S. & Reagan, M., 2020. Rapid subduction initiation and magmatism in the Western Pacific driven by internal vertical forces, *Nat. Commun.*, 11, 1874, doi:10.1038/s41467-020-15737-4.
- McKenzie, D.P., 1977. The initiation of trenches: a finite amplitude instability, in *Island Arcs Deep Sea Trenches and Barck-Arc Basins, of Maurice Ewing Series*, Vol. 1, pp. 57–61, eds Talwani, M. & Pitman, W.C., Am. Geophys. Un.
- Moresi, L.N., Dufour, F. & Mühlhaus, H.-B., 2003. A Lagrangian integration point finite element method for large deformation modeling of viscoelastic geomaterials, *J. Comp. Phys.*, **184**, 476–497.
- Mueller, S. & Phillips, R.J., 1991. On the initiation of subduction, *J. geophys. Res.*, **96**, 651–665.
- Muller, R.D. *et al.*, 2016. Global-scale plate reorganization events since Pangea breakup, *Annu. Rev. Earth planet. Sci.*, **44**, 107–138.
- Nikolaeva, K., Gerya, T.V. & Marques, F.O., 2010. Subduction initiation at passive margins: numerical modeling, *J. geophys. Res.*, 115(B3), doi:10.1029/2009JB006549.
- Patel, J., Sutherland, R., Gurnis, M., Van Avendonk, H., Gulick, S., Shuck, B., Stock, J. & Hightower, E., 2021. Stratigraphic architecture of Solander Trough records Southern Ocean currents and subduction initiation beneath southwest New Zealand, *Basin Res.*, 33(1), 403–426.
- Patriat, M. et al., 2015. Propagation of back-arc extension into the arc lithosphere in the southern New Hebrides volcanic arc, Geochem. Geophys. Geosyst, 16, 3142–3159.
- Patriat, M. et al., 2019. Subduction initiation terranes exposed at the front of a 2Ma volcanically-active subduction zone, Earth planet. Sci. Lett., 508, 30–40.
- Ranalli, G., 1995. Rheology of the Earth, Chapman and Hall.
- Reagan, M., Heaton, D., Schmitz, M., Pearce, J., Shervais, J. & Koppers, A., 2019. Forearc ages reveal extensive short-lived and rapid seafloor spreading following subduction initiation, *Earth planet. Sci. Lett.*, 506, 520–529.
- Ribe, N.M., 2001. Bending and stretching of thin viscous sheets, J. Fluid Mech., 433, 135–160.
- Seton, M. et al., 2016. Melanesian back-arc basin and arc development: constraints from the eastern Coral Sea, Gondw. Res., 39, 77–95.

- Shuck, B. et al., 2021. Strike-slip enables subduction initiation beneath a failed rift: new seismic constraints from Puysegur Margin, New Zealand, Tectonics. 40, 1–33.
- Shuck, B., Gulick, S., Van Avendonk, H., Gurnis, M., Sutherland, R., Stock, J. & Hightower, E., 2022. Stress transition from horizontal to vertical forces during subduction initiation, *Nat. Geosci.*, 15, 149–155.
- Stern, R. & Gerya, T., 2018. Subduction initiation in nature and models: a review, *Tectonophysics*, 746, 173–198.
- Stern, R.J., 2004. Subduction initiation: spontaneous and induced, *Earth planet. Sc. Lett.*, **226**, 275–292.
- Stern, R.J. & Bloomer, S.H., 1992. Subduction zone infancy: examples from the Eocene Izu-Bonin-Mariana and Jurassic California arcs, *Geol. Soc. Am. Bull.*, 104, 1621–1636.
- Sutherland, R., Barnes, P. & Uruski, C., 2006. Miocene-Recent deformation, surface elevation, and volcanic intrusion of the overriding plate during subduction initiation, offshore southern Fiordland, Puysegur margin, southwest New Zealand, New Zeal. J. Geol. Geophys. 49, 131–149.
- Sutherland, R. et al., 2017. Widespread compressional faulting associated with forced Tonga-Kermadec subduction initiation, Geology, 45, 355– 358.
- Sutherland, R. *et al.*, 2020. Continental scale of geographic change across Zealandia during subduction zone initiation, *Geology*, **48**, 419–424.

- Tarduno, J.A. *et al.*, 2003. The Emperor Seamounts: southward motion of the Hawaiian hotspot plume in Earth's mantle, *Science*, **301**, 1064–1069.
- Torsvik, T., Doubrovine, P., Steinberger, B., Gaina, C., Spakman, W. & Domeier, M., 2017. Pacific plate motion change caused the Hawaiian-Emperor Bend, *Nat. Commun.*, 8, doi:10.1038/ncomms15660.
- Toth, J. & Gurnis, M., 1998. Dynamics of subduction initiation at preexisting fault zones, *J. geophys. Res.*, **103**, 18 053–18 067.
- Turcotte, D.L. & Schubert, G., 1982. Geodynamics, Wiley.
- van Hinsbergen, D. J.J. *et al.*, 2015. Dynamics of intraoceanic subduction initiation: 2. Suprasubduction zone ophiolite formation and metamorphic sole exhumation in context of absolute plate motions, *Geochem. Geophys. Geosyst.*, **16**, 1–15.
- Watts, A.B., 2001. Isostasy and Flexure of the Lithosphere, pp. 458, Cambridge Univ. Press.
- Zhong, X. & Li, Z., 2019. Forced subduction initiation at passive continental margins: velocity driven versus stress-driven, *Geophys. Res. Lett.*, 46, 11054–11064.
- Zhou, X. & Wada, I., 2021. Differentiating induced versus spontaneous subduction initiation using thermomechanical models and metamorphic soles, *Nature Commun.*, 12, 1–31.
- Zhou, X., Li, Z.-H., Gerya, T., J. S.R., Xu, Z. & Zhang, J., 2018. Subduction initiation dynamics along a transform fault control trench curvature and ophiolite ages, *Geology*, 46, 607–610.

## SUPPORTING INFORMATION

Supplementary data are available at *GJI* online.

- Figure S1. (a)–(c) The effective viscosity [as  $\log_{10}(\eta_{\text{eff}})$ ] and the velocity vector from force boundary model  $F_{xx} = 9.24 \times 10^{12} \text{ N m}^{-1}$ . (d)–(f) The second invariant of stress  $\sigma_{\text{II}}$  [as  $\log_{10}(\sigma_{\text{II}})$ ] is colour-coded and overlain by the direction, from the same model as (a) to (c).
- Figure S2. (a) The normal force change  $N_b$  due to plate bending from velocity boundary models with different u but the same plate motion  $\ell$ (= 120 km). (b) Average viscosity  $\bar{\eta}$  (as  $\log_{10}\bar{\eta}$ ) from the same snapshots as (a). Panel (c)  $\log_{10}(\bar{\eta}u)$  from the same snapshots as (a). Due to plasticity,  $\bar{\eta} \sim \frac{1}{u}$ ,  $\bar{\eta}u$  is supposed to be a constant independent on u.
- **Figure S3**. The integration of pressure over depth in the lithosphere,  $F_p = \int_0^H p dz$ . Here the pressure p is the dynamic pressure (non-hydrostatic), and H the plate thickness. The plate boundary is at x = 450 km.
- **Figure S4**. The total work W done by  $F_{xx}$  with respect to plate motion  $\ell$  from velocity boundary models with different convergent rates with viscoplastic rheology(solid) and viscoplastic rheology(dotted).
- Figure S5.  $F_{xx}$  versus  $\ell$  from viscoelasto-plastic model with (a)  $\Delta t_{\ell} = 1$ Myr and (b)  $\Delta t_{\ell} = 1$ .5kyr  $\approx \Delta t$ . (a) is the same as Fig 4(c).
- **Figure S6**.  $F_{xx}$  versus  $\ell$  from viscoplastic model (solid) and viscoelasto-plastic model (dotted) with velocity boundary with yielding stress  $\tau_{\text{max}}$  equals: (a) 150 MPa, (b) 300 MPa, (c) 600 MPa and (d) 1200 MPa.
- **Figure S7**.  $\ell$  versus t from viscoplastic model (solid) and viscoelasto–plastic model (dotted) with force boundary with yielding stress  $\tau_{\text{max}}$  equals: (a) 150 MPa and (b) 300 MPa.
- **Figure S8.** Illustration of the hinge zone geometry and stress. The local coordinate system(s, z) is defined in Fig. 1. Two sectors draw the yielding area bounded by  $z = \pm z_1(s)$ . Every sector area is symmetric along the central axis  $s = s_c$ . Red, blue and green represent the central, edge and out of the yielding area.
- Figure S9. An example of measuring plate curvature k and its derivative  $\frac{dk}{ds}$  from numerical model. (a) The geometry of the plate. Red and green curves are the upper and lower interfaces of the mechanical plate measured from temperature contour T = 600 °C. Blue curve is the mid-point curve of the red and green curve. (b) Direct forward difference (orange) and TVRegDiff method(blue) of the blue curve in (a) direct forward difference (orange) and TVRegDiff method(blue) of the blue curve in (b). (d) Direct forward difference(orange) and TVRegDiff method(blue) of the blue curve in (c).

Please note: Oxford University Press is not responsible for the content or functionality of any supporting materials supplied by the authors. Any queries (other than missing material) should be directed to the corresponding author for the paper.

## APPENDIX A: FORCE BALANCE

Here we derive the force balance eq. (1). We start from Ribe (2001) eq. (2.5b) derived from the conservation of momentum and bending torque of a thin viscous sheet with constant plate thickness:

$$\frac{dN}{ds} = k \frac{dM}{ds} - Hg_s \delta \rho \left( 1 + \frac{k^2 H^2}{12} \right) - F_s^+ - F_s^- + \frac{1}{2} Hk(F_s^+ - F_s^-), \tag{A1}$$

where  $F_s$  reflect the component from plate surface traction in a curved plate,  $F_s^{\pm} = (\pm 1 - \frac{Hk}{2})T^{\pm}$  with a constant plate thickness and  $T^{\pm}$  is the shear traction at top and bottom surface of the plate. N and M are the plate normal force and plate bending moment. The component of gravity in the s direction is  $g_s$ , or  $g\sin\theta$ . Consequently, eq. (A1) yields

$$\frac{\mathrm{d}N}{\mathrm{d}s} = k \frac{\mathrm{d}M}{\mathrm{d}s} - Hg\sin\theta \delta\rho \left(1 + \frac{k^2H^2}{12}\right) - \left(\frac{Hk}{2} - 1\right)^2 T^+ + \left(\frac{Hk}{2} + 1\right)^2 T^-. \tag{A2}$$

From this equation we see that the changing of plate normal force can be decomposed into a bending, body and boundary force. The presence of the product Hk complicates the formulation, and Buffet (2006) states that Hk can be ignored as it is much smaller than 1, indicating the plate can function as a stress guide transmitting the stress in the s direction. The full numerical solutions show that the maximum plate curvature k can be as large as  $10^{-5}$  m<sup>-1</sup> (Fig. 8), so that the upper limit of Hk can be as large as 0.5, which is not negligible. However, the k reaches  $10^{-5}$  m<sup>-1</sup> only in the hinge zone area of well–developed subduction. For negative buoyancy term,  $\theta$  in the hinge zone is small. Shear traction  $T^{\pm}$  is significant only at the beginning of the subduction initiation, when plate curvature is small, but after subduction becomes well developed  $T^{\pm}$  becomes quite small in response to plate weakening. Therefore, the Hk term is negligible when both negative buoyancy and shear traction are dominant. With Hk vanishing, eq. (A2) simplifies to

$$\frac{\mathrm{d}N}{\mathrm{d}s} = k \frac{\mathrm{d}M}{\mathrm{d}s} - Hg \mathrm{sin}\theta \delta \rho - T^+ + T^-.$$

By integrating this equation from one end of the slab to the other, we obtain  $F_1 - F_2 = \int_0^L k dM - \int_0^L Hg \sin\theta \delta \rho ds + \int_0^L (T^- - T^+) ds$ . Further, with boundary conditions  $(F_2 = -F_{xx}, F_1 = -F_1)$  and substituting from eqs (2), (6), (7), (8) and (11), we obtain

$$F_{xx} + \Delta N_{NB} = \Delta N_b + T_s + F_a + F_I$$

verifying eq. (1).

## APPENDIX B: HINGE ZONE YIELDING

In eq. (3),  $\Delta N_b = K_b u + N_{\rm HZ}$ , we state that the bending torque  $\Delta N_b$  consist of two parts: A bending torque inside the hinge zone (independent of plate velocity) and one outside the hinge zone (proportional to plate velocity). Here we demonstrate this result. The shear stress within the bending slab,  $\tau_{ss}$  in the local coordinate system will be evaluated at centre, edge and outside of the hinge zone (red, blue and green cross sections in Fig. S8). Following Buffet (2006), we know that the strain rate in the bending area is  $\dot{\varepsilon}_{ss} = -zu\frac{dk}{ds}$ , where z and s are the local coordinate system. Outside the hinge zone, without plastic yielding the stress–strain relationship is linear  $\tau_{ss} = 4\eta\dot{\varepsilon}_{ss} = -4\eta zu\frac{dk}{ds}$ , and the moment is  $M = \int_{-\frac{H}{2}}^{\frac{H}{2}} \tau_{ss}z dz = -\frac{1}{3}H^3\eta u\frac{dk}{ds}$ . In the hinge zone, an upper limit is applied to the stress, so  $\tau_{ss} = \max(\min(-4\eta zu\frac{dk}{ds}, \tau_y), -\tau_y)$ . Near z = 0 the stress is small and so linear with strain rate and proportional to z, but with the yielding stress function as an upper limit for  $\tau_{ss}$  when |z| > 0. We define the intersect between a linear viscosity and plastic yielding as  $z = \pm z_1$ . The quantity  $z_1$  is a function of s,  $z_1 = z_1(s)$ , that in the centre of hinge zone the  $z_1$  is smallest, define as  $z_1 = z_1(s_c)$ . As  $z = z_1$  is the intersection of the linear viscosity with yielding, we have  $\tau_y = 4\eta z_1 u\frac{dk}{ds}$ , and we obtain  $z_1 = \frac{\tau_y}{4\eta u(y-\beta(s-s_c)^2)}$ , where  $\gamma$  and  $\beta$  are parameters to be determined. At the edge of the hinge zone, the boundary of yielding  $[z_1 = z_1(s)]$  intersects with the slab boundaries and  $z_1(s + s_{HZ}/2) = \frac{H}{2}$ . On the other hand, in the centre of the hinge zone, we have the smallest  $z_1$ , corresponding to a largest  $\frac{dk}{ds}$ . With these two constraints, we can evaluate  $\gamma$  and  $\beta$  to be  $\gamma = (\frac{dk}{ds})_{max}$  and  $\beta = ((\frac{dk}{ds})_{max} - \frac{\tau_y}{2\eta u})\frac{4}{s_{12}}$ . The derivation of total normal force change follows Buffet (2006),

$$\Delta N = \int_0^L k \mathrm{d}M = -\int_0^L M \mathrm{d}k,$$

where k is the plate curvature and M is the moment  $(M = \int_{-\frac{H}{2}}^{\frac{H}{2}} \tau_{ss} z dz)$ . The second part of the equation followings from the integration by parts, assuming k(s = 0) = k(s = L) = 0. By substituting the expression of M into the equation we obtain

$$\begin{split} &\Delta N = -\int_{0}^{L} \int_{-\frac{H}{2}}^{\frac{H}{2}} \tau_{ss} \frac{\mathrm{d}k}{\mathrm{d}s} z \mathrm{d}z \mathrm{d}s \\ &= -\int_{s \in C_{[0,L]}[s_{c} - \frac{s_{HZ}}{2}, s_{c} + \frac{s_{HZ}}{2}]} \int_{-\frac{H}{2}}^{\frac{H}{2}} \tau_{ss} \frac{\mathrm{d}k}{\mathrm{d}s} z \mathrm{d}z \mathrm{d}s - \int_{s_{c} - \frac{s_{HZ}}{2}}^{s_{HZ}} \int_{-\frac{H}{2}}^{\frac{H}{2}} \tau_{ss} \frac{\mathrm{d}k}{\mathrm{d}s} z \mathrm{d}z \mathrm{d}s \\ &= \int_{s \in C_{[0,L]}[s_{c} - \frac{s_{HZ}}{2}, s_{c} + \frac{s_{HZ}}{2}]} \frac{1}{3} H^{3} \eta u \left(\frac{\mathrm{d}k}{\mathrm{d}s}\right)^{2} \mathrm{d}s - \int_{s_{c} - \frac{s_{HZ}}{2}}^{s_{c} + \frac{s_{HZ}}{2}} \int_{-\frac{H}{2}}^{\frac{H}{2}} \max \left(\min \left(-4 \eta z u \frac{\mathrm{d}k}{\mathrm{d}s}, \tau_{y}\right), -\tau_{y}\right) z \frac{\mathrm{d}k}{\mathrm{d}s} \mathrm{d}z \mathrm{d}s \\ &= K_{L} u + N_{LZ} \end{split}$$

Here the integration is split into two parts: The first being the area outside the hinge zone where no plastic yielding occurs, and the second corresponds to the hinge zone bending torque  $N_{\rm HZ}$ . With symmetry, the second term can be further rewritten as

$$\begin{split} N_{\rm HZ} &= 2 \int_{s_c - \frac{s_{\rm HZ}}{2}}^{s_c + \frac{s_{\rm HZ}}{2}} \int_0^{\frac{H}{2}} \min \left( 4 \eta z u \frac{\mathrm{d}k}{\mathrm{d}s}, \tau_y \right) z \frac{\mathrm{d}k}{\mathrm{d}s} \mathrm{d}z \mathrm{d}s \\ &= 2 \int_{s_c - \frac{s_{\rm HZ}}{2}}^{s_c + \frac{s_{\rm HZ}}{2}} \int_0^{z_1} 4 \eta z^2 u \left( \frac{\mathrm{d}k}{\mathrm{d}s} \right)^2 \mathrm{d}z \mathrm{d}s + 2 \int_{s_c - \frac{s_{\rm HZ}}{2}}^{s_c + \frac{s_{\rm HZ}}{2}} \int_{z_1}^{\frac{H}{2}} \tau_y z \frac{\mathrm{d}k}{\mathrm{d}s} \mathrm{d}z \mathrm{d}s \\ &= 2 \int_{s_c - \frac{s_{\rm HZ}}{2}}^{s_c + \frac{s_{\rm HZ}}{2}} \frac{4}{3} \eta z_1^3 u \left( \frac{\mathrm{d}k}{\mathrm{d}s} \right)^2 \mathrm{d}s + 2 \int_{s_c - \frac{s_{\rm HZ}}{2}}^{s_c + \frac{s_{\rm HZ}}{2}} \frac{1}{2} \left( \frac{H^2}{4} - z_1^2 \right) \tau_y \frac{\mathrm{d}k}{\mathrm{d}s} \mathrm{d}s. \end{split}$$

With  $z_1 = \frac{\tau_y}{4nu(y-\beta(s-s_c)^2)}$ ,  $\frac{dk}{ds} = \gamma - \beta(s-s_c)^2$  the equation yields

$$\begin{split} &2\int_{s_{c}-\frac{s_{\mathrm{HZ}}}{2}}^{s_{c}+\frac{s_{\mathrm{HZ}}}{2}}\left(\frac{1}{8}H^{2}\tau_{y}\left(\gamma-\beta\left(s-s_{c}\right)^{2}\right)-\frac{\tau_{y}^{3}}{96\eta^{2}u^{2}\left(\gamma-\beta\left(s-s_{c}\right)^{2}\right)}\right)\mathrm{d}s\\ =&\frac{1}{48}\tau_{y}\left(H^{2}s_{\mathrm{HZ}}\left(12\gamma-\beta s_{\mathrm{HZ}}^{2}\right)-\frac{2\tau_{y}^{2}\mathrm{arctanh}\left[\sqrt{\frac{\beta}{\gamma}}\frac{s_{\mathrm{HZ}}}{2}\right]}{\sqrt{\beta\gamma}}\right). \end{split}$$

Recalling  $\beta = (\gamma - \frac{\tau_y}{2\eta Hu})\frac{4}{s_{yy}^2}$ , we obtain

$$N_{\rm HZ} = \frac{1}{6} \tau_y H^2 s_{\rm HZ} \gamma \left( 1 + \frac{\tau_y}{4 \gamma \eta H u} \right) - \frac{\tau_y^3 {\rm arctanh} \left[ \sqrt{\frac{\beta}{\gamma}} \frac{s_{\rm HZ}}{2} \right]}{24 \eta^2 u^2 \sqrt{\beta \gamma}}.$$

We can define a dimensionless quantity  $\zeta = \frac{z_1(s=s_c)}{z_1(s=s_c\pm\frac{3\mathrm{HZ}}{2})} = \frac{\tau_y}{2\gamma\eta Hu}$  which describe the ratio between minimum and maximum width of the non-yielding area in the hinge zone. With typical quantities from the models,  $\tau_y = 300$  MPa ( $\tau_{\mathrm{II}} \leq 150$  MPa),  $\gamma = 1 \times 10^{-10} \mathrm{m}^{-2}$  from Fig. 8, H = 60 km, u = 2 cm yr<sup>-1</sup> and  $\eta = 10^{25}$  Pa·s, we can estimate  $\zeta$  to be  $4 \times 10^{-3}$ . Therefore,  $\beta = (\gamma - \frac{\tau_y}{2\eta Hu})\frac{4}{s_{\mathrm{HZ}}^2} = (1 - \zeta)\frac{4\gamma}{s_{\mathrm{HZ}}^2} \approx \frac{4\gamma}{s_{\mathrm{HZ}}^2}$ .

$$\begin{split} N_{\rm HZ} &= \frac{1}{6} \tau_y H^2 s_{\rm HZ} \gamma \left(1+\zeta\right) - \frac{\tau_y^3 s_{\rm HZ} {\rm arctanh}[\sqrt{1-\zeta}]}{48 \gamma \, \eta^2 u^2} \\ &= \frac{1}{6} \tau_y H^2 s_{\rm HZ} \gamma \left(1+\zeta-\frac{\tau_y^2 {\rm arctanh}[\sqrt{1-\zeta}]}{8 \gamma^2 \eta^2 H^2 u^2}\right) \\ &= \frac{1}{6} \tau_y H^2 s_{\rm HZ} \gamma \left(1+\zeta-\frac{\zeta^2}{2} {\rm arctanh}[\sqrt{1-\zeta}]\right) \\ &\approx \frac{1}{6} \tau_y H^2 s_{\rm HZ} \gamma. \end{split}$$

The small  $\zeta$  indicates that plastic yielding pervasively occurs in the hinge zone, so that mostly the hinge zone has  $\tau_{ss} = \tau_y$ .